sid.inpe.br/mtc-m21c/2020/08.04.14.18-TDI

STATISTICAL STUDY OF THE CONTROL OF JUPITER'S DECAMETRIC RADIO EMISSIONS BY THE SATELLITE EUROPA

Hadassa Raquel Peixoto Jácome

Master's Dissertation of the Graduate Course in Space Geophysics/Science of the Solar-Terrestrial Environment, guided by Drs. Ezequiel Echer and Manilo Soares Marques, approved in May 28, 2020.

URL of the original document:
<http://urlib.net/8JMKD3MGP3W34R/4328C9L>

INPE
São José dos Campos
2020

PUBLISHED BY:

Instituto Nacional de Pesquisas Espaciais - INPE
Gabinete do Diretor (GBDIR)
Serviço de Informação e Documentação (SESID)
CEP 12.227-010
São José dos Campos - SP - Brasil
Tel.:(012) 3208-6923/7348
E-mail: pubtc@inpe.br

sid.inpe.br/mtc-m21c/2020/08.04.14.18-TDI

STATISTICAL STUDY OF THE CONTROL OF JUPITER'S DECAMETRIC RADIO EMISSIONS BY THE SATELLITE EUROPA

Hadassa Raquel Peixoto Jácome

Master's Dissertation of the Graduate Course in Space Geophysics/Science of the Solar-Terrestrial Environment, guided by Drs. Ezequiel Echer and Manilo Soares Marques, approved in May 28, 2020.

URL of the original document:
<http://urlib.net/8JMKD3MGP3W34R/4328C9L>

INPE
São José dos Campos
2020

Cataloging in Publication Data

Jácome, Hadassa Raquel Peixoto.

J153s Statistical study of the control of Jupiter's decametric radio emissions by the satellite Europa / Hadassa Raquel Peixoto Jácome. – São José dos Campos : INPE, 2020.

xxiv + 74 p. ; (sid.inpe.br/mtc-m21c/2020/08.04.14.18-TDI)

Dissertation (Master in Space Geophysics/Science of the Solar-Terrestrial Environment) – Instituto Nacional de Pesquisas Espaciais, São José dos Campos, 2020.

Guiding : Drs. Ezequiel Echer and Manilo Soares Marques.

1. Jupiter. 2. Radio emission. 3. Satellite Europa. 4. Control. 5. Decametric range. I.Title.

CDU 523.45:520.27

MINISTÉRIO DA CIÊNCIA, TECNOLOGIA E INOVAÇÕES
INSTITUTO NACIONAL DE PESQUISAS ESPACIAIS

FOLHA DE APROVAÇÃO

A FOLHA DE APROVAÇÃO SERÁ INCLUIDA APÓS RESTABELECIMENTO DAS ATIVIDADES PRESENCIAIS.

Por conta da Pandemia do COVID-19, as defesas de Teses e Dissertações são realizadas por vídeo conferência, o que vem acarretando um atraso no recebimento nas folhas de aprovação.

Este trabalho foi aprovado pela Banca e possui as declarações dos orientadores (confirmando as inclusões sugeridas pela Banca) e da Biblioteca (confirmando as correções de normalização).

Assim que a Biblioteca receber a Folha de aprovação assinada, esta folha será substituída.

Qualquer dúvida, entrar em contato pelo email: pubtc@inpe.br.

Divisão de Biblioteca (DIBIB).

"Lord, our Lord, how majestic is your name in all the earth! You have set your glory in the heavens. [...] When I consider your heavens, the work of your fingers, the moon and the stars, which you have set in place, what is mankind that you are mindful of them, human beings that you care for them? [...] Lord, our Lord, how majestic is your name in all the earth!"

Psalm 8

To my family.

ACKNOWLEDGEMENTS

I give thanks to God for having given me health and capability to strive for and obtain this accomplishment. To God be the glory.

I would also like to express my sincere thanks to INPE and to the professors of the Space Geophysics Postgraduate Program for the opportunity to work and study with highly qualified researchers, and for all the knowledge shared with me.

To CAPES and to FAPESP (grant 2019/03533-6) for the financial support.

To my advisors Dr. Ezequiel Echer and Dr. Manilo Soares Marques for their valuable assistance and guidance during the last years.

To Dr. Philippe Zarka for the availability and interest to read my work, and for all the comments and suggestions.

To the members of the examination board for having accepted the invitation to evaluate this work and for all the suggestions and remarks.

To my colleagues in INPE for the discussions and help during these two years.

To Dr. Gilvan Luiz Borba for having encouraged me to come to São José dos Campos for my postgraduate education at INPE.

To my family, especially my parents, for believing in me, for having always fought to give me conditions to pursue my dreams and for supporting me even from away. To my brothers and to my sister-in-law for the support. Thanks for loving me.

To my friends in São José dos Campos, specially to my housemates and to the Igreja Batista da Graça, for the hospitality, love and support.

To my friends outside São José dos Campos for checking up on me now and then.

Thank you!

ABSTRACT

Jupiter is an intense source of Auroral Radio Emissions (AREs). Such emissions originate from resonance between non-relativistic electrons gyrating along Jupiter's magnetic field lines and electromagnetic waves, in the Cyclotron maser instability. The jovian AREs in the Decametric (DAM) wavelength range can be detected from ground-based instruments on the Earth for having frequencies that surpass the cut-off frequency of the Earth's ionosphere. The occurrence of the jovian AREs is partially controlled by the Galilean satellites Io, Europa and Ganymede. The satellite control occurs by emissions' induction through field-aligned electric currents resulting from the interaction between the satellites and the magnetospheric plasma along their orbit. Evidence of this control is the nonuniform occurrence of jovian DAM emissions along the satellites' orbital phase and the observer's longitude. Such evidence was firstly observed in 1955 for Io and has been found also for Ganymede and for Europa. The continuous observation of Jupiter's radio emissions by the Nançay Decameter Array (NDA) along the years has enabled the gathering of an extensive digital data catalog with 29 years of daily observations. This catalog has already provided statistical evidences of the control of the jovian DAM emissions by Io and Ganymede, as well as the possibility of further selection and analysis of emissions. This work main objective was to analyze this NDA's catalog to select and analyze jovian DAM emissions possibly induced by the satellite Europa. As results, we were able to detect and characterize possible Europa-induced (Eu-DAM) emissions from two different sources, A and C, on Jupiter. Statistical distribution parameters, such as the median, mean and standard deviation, for these emissions' maximum frequency, duration and intensity have been found for the first time. Main maximum frequency ranges of the analyzed Eu-DAM emissions were suggested. Moreover, the Eu-A and Eu-C emissions selected in this work were also compared with the Eu-A and the Eu-C emissions observed in previous works on the databases of the Voyagers 1 and 2 and Cassini, and with Io- and Ganymede-induced emissions on the NDA's catalog.

Keywords: Jupiter. Radio emission. Satellite Europa. Control. Decametric range.

ESTUDO ESTATÍSTICO DO CONTROLE DAS EMISSÕES DECAMÉTRICAS DE RÁDIO DE JÚPITER PELO SATÉLITE EUROPA

RESUMO

Júpiter é uma intensa fonte the Emissões Aurorais de Rádio (AREs, do inglês *Auroral Radio Emissions*). Essas emissões são geradas por ressonância entre elétrons não relativísticos presos às linhas de campo magnético do planeta e ondas eletromagnéticas no plasma, na instabilidade maser ciclôtronica. As emissões AREs jovianas com comprimento de onda Decamétrico (DAM) podem ser detectadas por instrumentos localizados na superfície da Terra por terem frequências superiores à frequência de corte da ionosfera terrestre. A ocorrência das emissões AREs de Júpiter é parcialmente controlada pelos satélites Galileanos Io, Europa e Ganimedes. O controle por satélite ocorre pela indução de emissões por correntes elétricas alinhadas ao campo magnético resultantes da interação entre os satélites e o plasma magnetosférico ao longo de sua órbita. É evidência desse controle a ocorrência não uniforme de emissões jovianas ao longo da fase orbital de satélites e da longitude do observador. Tal evidência foi primeiramente observada em 1955 para Io e já foi observada também para Ganimedes e para Europa. O contínuo funcionamento da rede de antenas decamétricas de Nançay (NDA, do inglês *Nançay Decameter Array*) ao longo dos anos tem possibilitado a compilação de um extenso catálogo digital com 29 anos de observações diárias de Júpiter. Este catálogo tem fornecido evidências estatísticas do controle das emissões decamétricas de Júpiter por Io e Ganimedes, como também a possibilidade de seleção e análise de emissões. Este trabalho teve como principal objetivo a análise do catálogo da NDA para selecionar e analisar emissões DAM jovianas possivelmente induzidas pelo satélite Europa. Como resultados, foi possível detectar e caracterizar emissões possivelmente induzidas por Europa (Eu-DAM) com origem em duas fontes distintas em Júpiter, A e C. Parâmetros estatísticos de distribuição, como a média, mediana e desvio padrão, foram calculados pela primeira vez para a frequência máxima, a duração e a intensidade destas emissões. Foram sugeridos intervalos de máxima frequência dominantes das emissões Eu-DAM analisadas. Além disso, as emissões Eu-A e Eu-C selecionadas neste trabalho foram comparadas com as emissões Eu-A e Eu-C observadas em estudos anteriores nas bases de dados das sondas Voyagers 1 e 2 e Cassini, e com emissões induzidas por Io e por Ganimedes presentes no catálogo da NDA.

Palavras-chave: Júpiter. Emissões de rádio. Satélite Europa. Controle. Faixa decamétrica.

LIST OF FIGURES

Page

LIST OF TABLES

Page

LIST OF ABBREVIATIONS

ARE	–	Auroral Radio Emission
DAM	–	Decametric
HOM	–	Hectometric
bKOM	–	broadband Kilometric
nKOM	–	narrowband Kilometric
IR	–	Infrared
UV	–	Ultraviolet
FUV	–	Far-Ultraviolet
NDA	–	Nançay Decametric Array
HST	–	Hubble Space Telescope
STIS	–	Space Telescope Imaging Spectrograph
ExPRES	–	Exoplanetary and Planetary Radio Emission Simulator
CMI	–	Cyclotron Maser Instability
CML or LCM	–	Central Meridian Longitude
LH	–	Left Hand sense
RH	–	Right Hand sense
NH	–	Northern Hemisphere
SH	–	Southern Hemisphere

LIST OF SYMBOLS

R_J	–	Jupiter's radius ($R_J = 71492$ km)
$\vec{B}$	–	background magnetic field vector
$\vec{V}$	–	plasma's velocity vector
$\vec{V}_A$	–	Alfvén velocity vector
ω_p	–	plasma frequency ($\omega_p = 2\pi f_p$)
ω_c	–	cyclotron frequency ($\omega_c = 2\pi f_c$)
$\vec{k}$	–	wave vector
ω	–	wave frequency
ω_i	–	growth rate
γ	–	Lorentz factor
θ	–	beaming cone's mid-aperture angle
α	–	loss-cone's mid-aperture angle
Φ_{Sat}	–	satellite's orbital phase
Λ_{Sat}	–	satellite's longitude
δ_a	–	the lead angle

CONTENTS

Page

1 INTRODUCTION

Jupiter is a powerful source of Auroral Radio Emissions (AREs), which were first detected from the planet in 1955 (BURKE; FRANKLIN, 1955). Since then, these emissions have been an important tool in the study of Jupiter's magnetic field, magnetosphere and rotation rate, as well as of the physical processes occurring in the jovian magnetosphere (ZARKA, 1998). Nowadays, it is known that Jupiter has a strong magnetic field, which configures the largest planetary magnetosphere in the Solar System, with the subsolar magnetopause reaching distances of $45 - 100$ R_J[1] (KHURANA et al., 2004; BAGENAL, 2007; ECHER, 2010).

The origin of the AREs is commonly associated with the interaction between non-relativistic energetic electrons out of equilibrium gyrating along magnetic field lines and a rotating electric field, by the Cyclotron Maser Instability (CMI) (ZARKA, 1998). The occurrence of the CMI in Jupiter's magnetosphere was suggested based on properties shared by the observed jovian Decametric (DAM) emissions, as: the brightness temperatures higher than 10^{15} K; the frequency of emission, which is close to the local electron cyclotron frequency (ω_c) in high magnetic latitudes, where the plasma frequency (ω_p) is much smaller than ω_c, $\omega_p/\omega_c \ll 1$; the polarization in circular or elliptical modes; and the large angles between their beaming and the magnetic field (CLARKE et al., 2004). The DAM range, which receives that name because of the wavelengths of tens of meters of its corresponding waves, is the only radio frequency range from Jupiter that can be observed from the ground since it reaches frequencies up to 40 MHz, surpassing the cut-off frequency of the Earth's ionosphere ($\sim$ 10 MHz) (CLARKE et al., 2004). For this reason, the jovian DAM were the first emissions detected from Jupiter and the only planetary emissions that we could observe until the start of spacecraft in situ observations on Earth, above the ionosphere, and on other magnetized planets, as Jupiter.

Through analyses of the jovian DAM, indications of control of the emissions by satellites orbiting Jupiter have been identified. The first observed effect of satellites on Jupiter auroral activity was the modulation of part of the jovian DAM by the satellite Io, presented in the 1960s by Bigg (1964). This discovery gave rise to discussions about the occurrence of an electromagnetic interaction connecting the satellites to Jupiter and whether the other satellites could also affect the occurrence of emissions in DAM and other ranges. Several models have been suggested to explain that interaction thereafter (PIDDINGTON; DRAKE, 1968; GOLDREICH; LYNDEN-BELL, 1969;

[1] Jupiter's radius (R_J) is equivalent to 71492 km.

GOERTZ, 1980; NEUBAUER, 1980; CRARY; BAGENAL, 1997). However, with regard to the control by satellites other than Io, no evidence was found until the observations from Voyager-1 and 2, Galileo and Cassini spacecraft, whose data showed the control of jovian radio emissions by the satellites Ganymede, Europa and, more slightly, Callisto (DULK, 1967; HIGGINS et al., 2006; HIGGINS, 2007; LOUIS et al., 2017).

Io, Europa, Ganymede and Callisto are the largest satellites orbiting Jupiter and are referred to as the Galilean satellites after Galileo Galilei, who first observed them, in 1610. Io is the closest Galilean satellite to Jupiter (at a radial distance of 5.9 R_J from the jovian center) and is the main source of plasma within its magnetosphere, providing, by volcanic activity, $\sim$ 1 ton/s of plasma to the magnetosphere. This large amount of plasma accumulates in a dense plasma torus which extends from 5.2 R_J to $\sim$ 10 R_J, at the magnetic equator (BAGENAL; SULLIVAN, 1981; KHURANA et al., 2004; KRUPP et al., 2010). Europa (at 9.4 R_J), Ganymede (at $\sim$ 15 R_J) and Callisto (at $\sim$ 26.4 R_J) are ice-covered and, by surface sputtering, also provide plasma to the magnetosphere, but in a much smaller scale, estimated to be less than $\sim$ 20 kg/s (KHURANA et al., 2004). The plasma density and magnitude of the magnetic field in the vicinity of these satellites, both decreasing in the magnetosphere with the distance from Jupiter, are thought to be some of the main reasons for their effect on the radio emissions to be weaker than Io's (DULK, 1967) and, thus, more difficult to be observed.

Nowadays, besides the spacecraft data, the detection of evidences for the control of the jovian AREs by Ganymede and of indications of control by Europa has been enabled by the extended catalog of the Nançay Decameter Array (NDA), which assembles 29 years of digitally recorded daily observations of Jupiter in the DAM range. This catalog has enabled not only the detection of evidences of the satellite control of the jovian DAM, but also the selection of possible satellite-induced emissions (Io-DAM or Ga-DAM for the emissions dependent of Io or Ganymede, respectively) for statistical analysis of their characteristics, as maximum frequency, duration, intensity, and sources. So far, only the Io-DAM and the Ga-DAM on the NDA's catalog were selected and characterized.

Based on that, the main objective of this work is to investigate the control of Jupiter's non-Io and non-Ga DAM emissions by Europa on the NDA's extensive catalog, following the work of Marques et al. (2017) and as a continuation of the work of Zarka et al. (2017). Further, possible Eu-DAM emissions will be selected and characterized with regard to their sources on Jupiter, maximum frequency, duration

and intensity.

This work is organized in the next chapters as follows:

- Chapter 2 contains a brief presentation of the jovian auroral radio emissions: the main, the polar and the satellite auroras. The satellite aurora occurs at the base of the satellites' flux tube on Jupiter's atmosphere and results from the Jupiter-satellite electrodynamic interaction. Therefore, it is the type of aurora controlled by the satellites. Also, the discovery of this control on part of the jovian DAM is briefly discussed in this chapter, and some of the models that were thereafter suggested to explain the control are presented.

- Chapter 3 discusses about the satellite Europa, which is the Galilean satellite whose control over the jovian DAM emissions is analyzed in this work. Evidences of an Earth-like ocean in Europa and a brief review on the search for the control of the jovian radio emissions by this satellite along the years are presented.

- Chapter 4 brings a review on the theoretical deduction of the Cyclotron Maser Instability (CMI), which is the mechanism responsible for the origin of the known planetary auroral radio emissions, by plasma wave amplification.

- Chapter 5 discusses about characteristics of the events' observation, which result from the beaming conditions and the rotation system. The parameters that are important for the analysis of this work, as the satellite's phase angle and Jupiter's Central Meridian Longitude (CML), as well as the classification of the possible sources, are presented in this chapter. Later, the extensive catalog of jovian DAM emissions that is analyzed in this work, and the instrumentation responsible for the data acquisition, the Nançay Decameter Array (NDA), are presented.

- Chapter 6 shows the initial processing and analysis of the NDA's catalog data. The analysis is statistical and intends to select the intervals of CML and Europa's phase where good correlation between the events' occurrence probability and the Europa's orbital phase is observed.

- Chapter 7 brings the analysis of characteristics of the emissions occurring within the selected intervals of good correlation and the selection of the

emissions possible induced by Europa. Special attention is given to the maximum frequency of the emissions. The chapter ends with a comparison between the Eu-DAM selected in this work and some of the Ga-DAM and Io-DAM on the NDA's catalog.

- Chapter 8 presents the conclusions of this work and future prospects.

2 JUPITER'S AURORAL RADIO EMISSION

Radio emissions have been detected from all the magnetized planets in our Solar system: Earth, Jupiter, Saturn, Uranus, and Neptune. These emissions are originated on the planets' auroral regions, at high magnetic latitudes, and are, therefore, referred to as planetary Auroral Radio Emissions (AREs). The frequency ranges of the known planetary AREs and their respective flux density at a distance of 1 AU from their sources (1 AU $\approx 1.5 \times 10^8$ km) are presented in Figure 3.5. From the figure, it is observed that Jupiter is the planet with the broadest frequency range of AREs, which reflects the high intensity of the planet's magnetic field (ZARKA, 1998). The jovian AREs have frequencies up to 40 MHz, which enable the detection of the parcel of them with the highest frequencies (> 10 MHz) by instruments on the Earth's surface (ZARKA, 1998; CLARKE et al., 2004). This parcel corresponds to the majority of the jovian Decametric (DAM) emissions.

Figure 2.1 - Flux density vs. frequency of the known planetary auroral radio emissions.

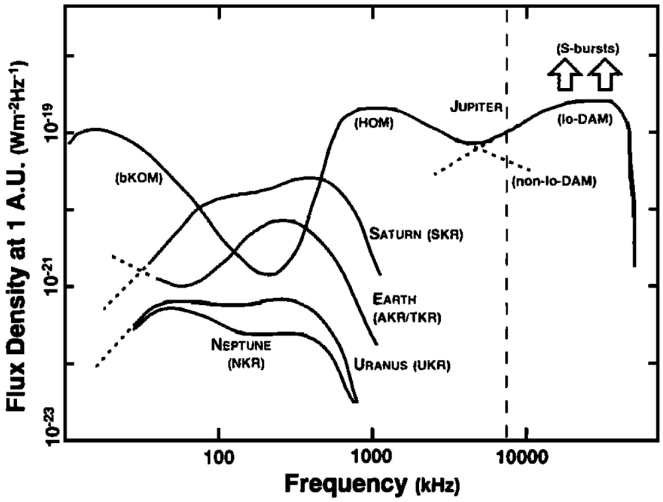

The flux densities are normalized to a distance of 1 AU from the sources. The KRs stand for Kilometric Radiation. The vertical dashed line indicates approximately the cut-off frequency of the Earth's ionosphere.

SOURCE: Zarka (1998).

The non-thermal radio emissions of Jupiter have been known since 1955, when Burke and Franklin (1955) observed DAM emissions and associated them with the planet. This discovery was also the first evidence for a planetary magnetosphere other than Earth. Besides the DAM emissions, lower frequency bands of Jupiter radio emissions

were first observed by the Voyager 1 and 2, in 1979. The spacecraft identified hectometric (HOM) emissions, with frequencies ranging from 200 kHz to a few MHz; broadband kilometric (bKOM) emissions, from $\sim$ 10 kHz to $<$ 1 MHz; and narrowband kilometric (nKOM) emissions, from 100 kHz to 200 kHz (CARR et al., 1983; CLARKE et al., 2004).

These emissions are originated on the polar regions of Jupiter and are related to physical processes occurring in different regions of the magnetosphere: inner ($< 10\ R_J$); middle (10–40 R_J); and outer ($> 40\ R_J$). The connection of the jovian poles to those regions in the magnetosphere is set through field-aligned currents (Birkeland currents) that close the electric currents in the magnetosphere to ionospheric currents, as shown in Figure 2.2. The magnetospheric dynamics phenomena associated with the auroral emissions are indicated by features of the emissions, as the magnetic co-latitude of their sources, their variability and rotation period. The emissions are, then, separated in three groups by their source region: the main oval aurora; the polar aurora; and the satellite aurora (CLARKE et al., 2004; BAGENAL, 2007; BAGENAL et al., 2017). The occurrence regions of these three auroral emission types are indicated in Figure 2.3, which shows the North pole of Jupiter in an image in the UV region, taken by the Space Telescope Imaging Spectrograph (STIS), in 26 November 1998.

The main oval is located around the magnetic poles at the magnetic co-latitude of $\sim 15^\circ$ and has approximately continuous emissions, with only slight variations in intensity. These emissions are controlled by the magnetic field and are related to the breakdown of the magnetospheric plasma's corotation in the middle magnetosphere (at $\sim 20\ R_J$) and to the jovian ionosphere's attempt to maintain the corotation through electric currents that transmit the ionospheric angular momentum. The polar aurora is the most variable among all the types of jovian aurora and occurs poleward from the main oval. The polar emissions are mostly related to physical processes occurring in closed magnetic field lines in the middle and outer magnetosphere, but are also controlled by the solar wind and the jovian local time, being more intense at the dusk side (KHURANA et al., 2004; CLARKE et al., 2004; BAGENAL, 2007).

The satellite-controlled aurora reflects physical processes occurring in the inner and middle magnetosphere due to the interaction between the magnetospheric plasma and Jupiter's satellites. The source region of the satellite aurora is located equatorward of the main oval and is composed by a bright spot at the satellite's footprint

followed by a faint trail downstream of the satellite, where non-thermal radio DAM emissions are observed (CLARKE et al., 2004; BAGENAL et al., 2017). Part of the satellite aurora radio emissions is also affected by the solar wind's variations (as some emissions in the kilometric, hectometric and DAM ranges) (CLARKE et al., 2004; ECHER et al., 2010; HESS et al., 2012). This type of aurora has been observed on the footprints of Io, Europa, Ganymede and possibly Callisto (CLARKE et al., 2002; BHATTACHARYYA et al., 2018). Io's, Ganymede's and Europa's footprints are indicated in Figure 2.3. This work focus on the satellite aurora, since we intend to study the control of DAM emissions by Europa.

Figure 2.2 - Meridian cross section of the jovian magnetosphere with a representation of an electric current system connecting the equatorial plasma in the magnetosphere to the jovian ionosphere.

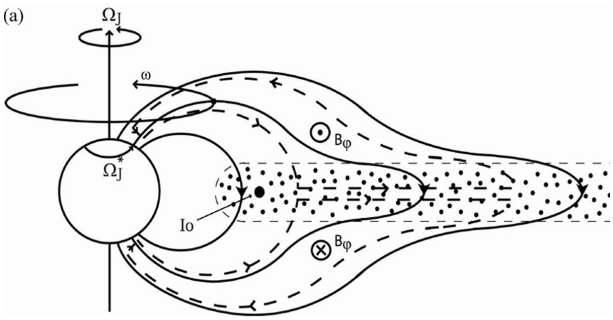

The solid lines with arrows represent the magnetic field lines, that are dragged by the plasma flowing away from Jupiter. The dashed lines with arrows represent the electric currents that are closed in the jovian ionosphere. The dotted region is the plasma sheet in the magnetosphere, which starts around the Io's plasma torus region. Ω_J is the angular velocity of Jupiter; Ω_J^*, the angular velocity of the Pedersen layer in the ionosphere; and ω, the angular velocity of a magnetic field shell. B_ϕ is the azimuthal component of the magnetic field, originated due to the bend of the field lines.

SOURCE: Clarke (2012).

The control of part of the jovian non-thermal radio emissions by the satellites was early observed by Bigg in 1964, but only for the satellite Io, and has been a strong evidence of the Io-Jupiter electrodynamic interaction. Much effort has been applied to understand this interaction from what is already known about Jupiter's magnetosphere, plasma physics, and the Earth's and Jupiter's auroral observations. A brief review of the first indications of control of jovian radio emissions by satellites that orbit Jupiter and some of the models suggested to explain the satellite-planet interaction are presented in the following sections.

Figure 2.3 - Footprints of Io, Ganymede and Europa on Jupiter's atmosphere.

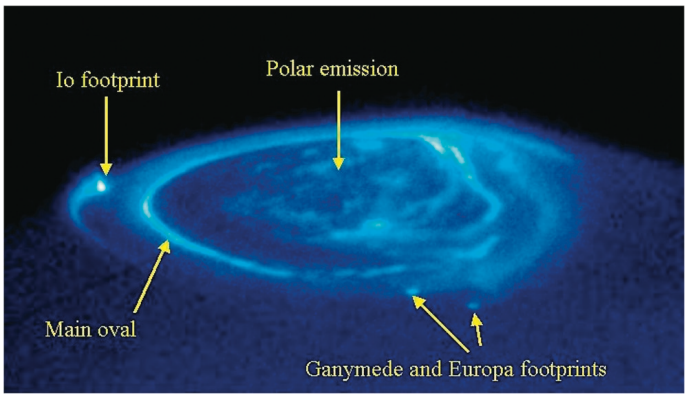

Image in the UV region, taken by the STIS on the 26 Nov. 1996, showing the three regions of auroral emissions on the North pole of Jupiter.

SOURCE: Clarke (2012).

2.1 Control of Jupiter's radio emission by satellites

The dependence of part of Jupiter's DAM emissions on Io's location was first suggested by Bigg (1964), who observed that the orbital phase of Io is relevant to the occurrence of the emissions. Bigg plotted the Jupiter's DAM emissions detected in the years 1961, 1962 and 1963 as a function of Io's orbital position (Φ_{Io}), and observed a modulation of the emissions' occurrence, with peaks on $\Phi_{Io} \simeq 90°$ and $\Phi_{Io} \simeq 250°$, as it is shown in Figure 2.4. The data was managed in a such way to accentuate the more intense emissions, yet the modulation could be observed even without it. This observation was an indication of the electromagnetic interaction between Jupiter and Io, which was later inferred to be also the cause of the bright spots in Io's footprint in Jupiter's atmosphere, detected in images in the far-ultraviolet (FUV) region taken with the Faint Object Camera on the Hubble Space Telescope (HST) (PRANGÉ et al., 1996).

Similarly, the identification of ultraviolet (UV) emissions from the footprints of Ganymede and Europa indicated the existence of the same electromagnetic interaction between each one of these satellites and Jupiter, and also the possibility of influence of their location on the occurrence and intensity of Jupiter's DAM emissions. Figure 2.3 shows UV bright spots observed in Io's, Ganymede's and Europa's footprints in Jupiter's atmosphere (CLARKE et al., 2002; CLARKE, 2012).

The first evidences of control of part of the jovian DAM emissions by Ganymede were

observed by Menietti et al. (1998) on data from Galileo spacecraft. The analyzed emissions had frequencies from 3.2 MHz to 5.6 MHz and presented enhancement of occurrence probability when Ganymede was in orbital phases of $\sim 80°$ and $\sim 245°$. Similar results were observed more recently by Louis et al. (2017), who simulated satellite-induced emissions' arcs on dynamic spectra and compared them with real data from the Cassini and Voyager 1 and 2 spacecraft. The spacecraft data was also source of evidence of control of part of the DAM emissions from Jupiter by Europa (see Section 3.2).

Figure 2.4 - Modulation of Jupiter's DAM emissions as a function of Io's orbital position.

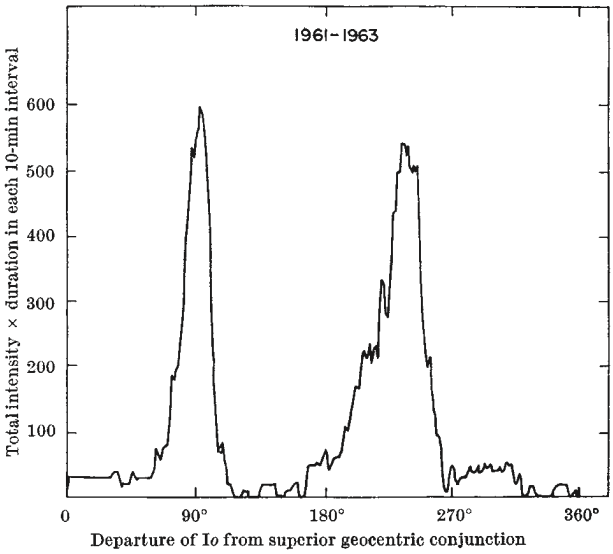

Emissions with maximum frequency ≥ 30 MHz. The events occur predominantly when Io is at $\sim 90°$ or at $\sim 250°$ on its orbit.

SOURCE: Bigg (1964).

Moreover, the extended catalog of DAM emissions observed by the ground-based Nançay decameter array since 1990 has enabled the observation of the jovian DAM control by the satellites Io and Ganymede and confirmed the results of studies with spacecraft data (MARQUES et al., 2017; ZARKA et al., 2017; ZARKA et al., 2018).

2.2 Satellite-Jupiter electrodynamic interaction

Based on the control of part of jovian DAM radio emissions by Io, different models have been proposed to explain the origin of field-aligned currents capable of causing

electron acceleration and precipitation in Io's footprint on Jupiter's atmosphere. These models may also be applied to the other Galilean satellites, such as Europa.

2.2.1 The unipolar inductor model

The unipolar inductor model was suggested by Piddington and Drake (1968), and Goldreich and Lynden-Bell (1969). It consists of a steady current loop along the magnetic field lines, closing through Jupiter's ionosphere and Io's interior and/or ionosphere, which acts as a unipolar inductor. According to this model, a magnetic flux tube connects Jupiter to Io, which is assumed to be a good electrical conductor. The plasma inside the flux tube tends to flow as attached to Io and, consequently, an electric field appears in Jupiter's rest frame. The resulting electric currents are, then, dependent on the conductivity of Jupiter's ionosphere and flow along the flux tube through Alfvén waves toward the satellite. There, the currents cross the flux tube and flow back to Jupiter. The complete circuit in the meridian plan is represented in Figure 2.5, where the direction of the currents is indicated by the arrows along the edges of the flux tube and in the interior of Io.

Figure 2.5 - Representation of the steady state circuit connecting Io and Jupiter.

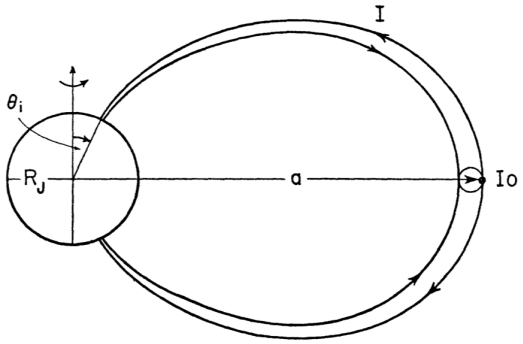

SOURCE: Goldreich and Lynden-Bell (1969).

The steady state is accomplished when the Alfvén wave completes the entire round trip between Jupiter's ionosphere and Io. Therefore, it is necessary that the wave travels fast enough to encounter the satellite after the trip back to Io from the ionosphere. If the displacement of the flux tube during the wave's travel time is greater than Io's diameter, the circuit is not closed (GOLDREICH; LYNDEN-BELL, 1969).

2.2.2 The Alfvén wing model

Upon the discovery of Io's dense plasma torus, Goertz (1980) and Neubauer (1980) suggested a model of electrodynamic interaction not dependent on the conductivity of Jupiter's ionosphere, but based on pickup and Alfvén waves instead. The pickup process refers to the acceleration of newly created ions in the vicinity of the satellite. The ions could result from photoionization and/or impact of the ambient plasma with neutrals in Io's atmosphere. The acceleration of the fresh ions to corotation results in the pickup current, which propagates along the magnetic field line through Alfvén waves (GOERTZ, 1980).

The Alfvén waves carry not only the pickup current but also the electric current resulted from the slowing of the plasma flow and the deviation of the magnetic field lines as the plasma approaches the satellite and passes by it. The field and plasma perturbation region is bordered by the Alfvén waves and, in the satellite's rest frame, appears in a wedge-shaped structure, referred to as Alfvén wing (KIVELSON et al., 2004). Figure 2.6 shows sketches of the Alfvén wing's structure in two different cuts, where the vectors for the plasma's velocity at the satellite's rest frame and the ambient magnetic field are represented by v and B, respectively.

Figure 2.6 - Representation of the Alfvén Wing.

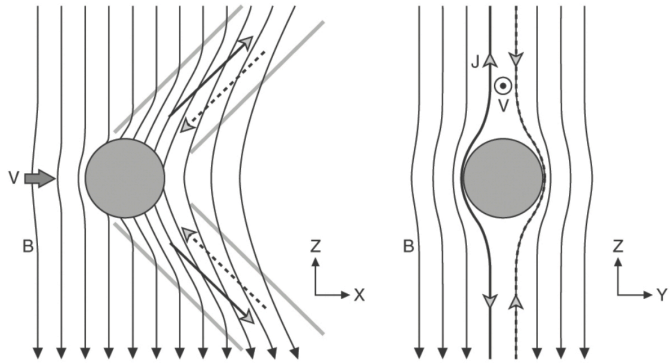

V is the vector of the plasma's velocity relative to the satellite and **B**, the magnetic field frozen in the plasma. Jupiter is located "behind" the V×B plane on the left. On the right, Jupiter is to the right. The flux tubes outside the Alfvén wing do not encounter the satellite, but are deflected from it.

SOURCE: Kivelson et al. (2009).

The Alfvén waves propagate with a group velocity given by

$$\vec{V}_A^{\pm} = \vec{V} \pm \frac{\vec{B}}{(\mu_0 \rho)^{1/2}} \tag{2.1}$$

where $\vec{V}$ is the plasma's velocity; $\vec{B}$, is the magnetic field vector; ρ, is the plasma's mass density; and the plus and the minus signs refer to the wave propagation along $\vec{B}$ and in opposite direction to $\vec{B}$, respectively (NEUBAUER, 1980). From equation 2.1 and considering Io's dense plasma torus, Neubauer (1980) proposed that the Alfvén waves must be reflected upon strong variations of plasma density in the magnetosphere: not only at Jupiter's ionosphere but also at the torus' boundaries, and that the waves would propagate slowly inside of the torus, not returning to Io after the reflection. In this context, the return of Alfvén waves to Io would be more easily accomplished when Io is at its maximum or minimum magnetic latitudes, possibly out of the torus, where the group velocity of the Alfvén waves would be higher. There, the Io-Jupiter coupling would be more strongly established. Figure 2.7 shows the expected behaviour of the Alfvén waves when Io is within and outside its plasma torus.

Figure 2.7 - Representation of the reflection of the Alfvén waves at the torus' boundary and at Jupiter's ionosphere.

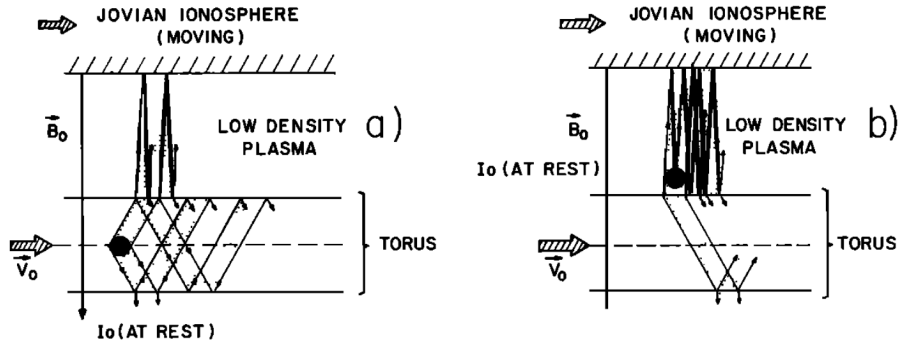

In (a), the interaction is shown for when Io is inside the plasma torus. The reflected waves do not reach the satellite. In (b), Io is out of the torus, at its maximum magnetic latitude. In this case, the waves may reach Io after reflection.

SOURCE: Neubauer (1980).

2.2.3 The Alfvén wave with steady state interaction model

Crary and Bagenal (1997) proposed that the interaction between Io and Jupiter could not be described by the Alfvén model or the unipolar inductor model alone, but by a composition of both occurring in different phases. From the time spacing of the jovian DAM arcs on time-frequency diagrams, the authors implied that the emissions must be caused by Alfvén waves propagating back and forth between Jupiter's ionosphere and the boundary of the torus instead of going all the way to Io as earlier suggested by Gurnett and Goertz (1981).

According to Crary and Bagenal (1997), the interaction begins with an alfvénic disturbance when magnetic field lines first reaches Io, as it is described by Goertz (1980) and Neubauer (1980), and then evolves into the steady current of Goldreich and Lynden-Bell (1969) through the waves trapped in the high magnetic latitudes. The propagation of the Alfvén waves in this model is presented in Figure 2.8 and may be compared with the model of Gurnett and Goertz (1981).

Figure 2.8 - Representation of the propagation of reflecting Alfvén waves trapped between the outer boundary of Io's torus and Jupiter's ionosphere.

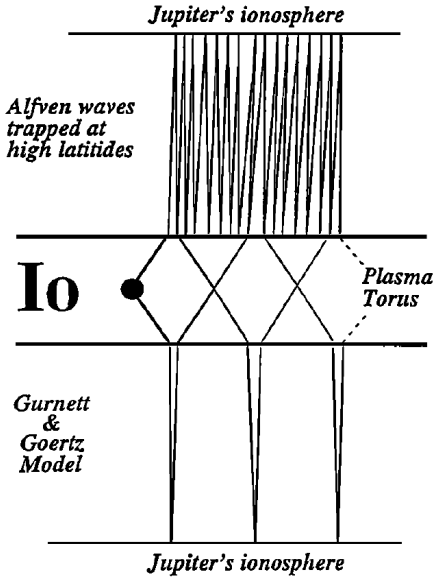

The propagation model suggested by Crary and Bagenal (1997) is shown in the up part and is compared with the model suggested by Gurnett and Goertz (1981), on the bottom part.

SOURCE: Crary and Bagenal (1997).

2.3 Generation of the satellite-induced DAM radio emissions

A scenario for the production of the radio emissions at the footprint and wake of the satellites was suggested based on analyses of the S-bursts originated at Io's footprint. S-bursts are millisecond impulsive radio emissions ("S" for "Short") which correspond to only 10% of the jovian DAM radio emissions and are characterized by frequency drift, usually from high to low frequencies. It was found that the occurrence of S-bursts is anticorrelated to the intensity of the UV and IR emissions at the satellite's footprint. This anticorrelation indicates that the S-burst are produced by particles with unstable velocity distribution traveling away from Jupiter. The initial Alfvén waves carry electron beams that precipitate in Jupiter's atmosphere and causes UV and IR emissions. The electrons out of the loss cone are not lost, but propagate back to the satellite with unstable loss-cone distribution. These electrons contribute to the CMI, providing the energy to drive wave amplification. Consequently, the more electrons precipitating in the atmosphere, more UV and IR emissions and less S-bursts will happen. (DULK, 1985; ZARKA et al., 1996; CRARY, 1997; CLARKE et al., 2004; SAUR et al., 2004; ERGUN et al., 2006). Figure 2.9 brings a sketch of the CMI beaming cone (radiation cone) from which the radio jovian DAM are emitted, in a flux tube. The CMI beaming cone is mathematically described in the Chapter 4.

Figure 2.9 - Sketch of loss cones and the radio emissions' beaming cone in a flux tube.

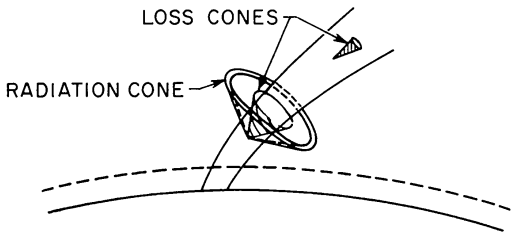

Radio emission by CMI is driven by free energy from electrons out of the loss cone moving along the magnetic field lines.

SOURCE: Dulk (1985).

The longest component of the DAM, the L-burst, is called "Long" for varying more slowly than the S-bursts, from minutes to hours (ZARKA et al., 1996). The L-bursts are not produced by the initial Alfvén wave, but by a steady system of currents propagating upward and downward Jupiter's ionosphere along Io's wake. The energy for the generation of the L-bursts by the CMI would come from particles with

unstable distributions in the upward currents (CRARY; BAGENAL, 1997; SU et al., 2003; BAGENAL, 2007). Figure 2.10 shows the regions of occurrence of the S- and L-bursts and the directions of the currents associated with them. The characteristics shared by both the Io-DAM and the non-Io-DAM suggest that they are generated by the same mechanism, but occurring at different temporal and/or spatial conditions (SAUR et al., 2004).

Figure 2.10 - Io's footprint and wake regions and the particle-accelerating currents.

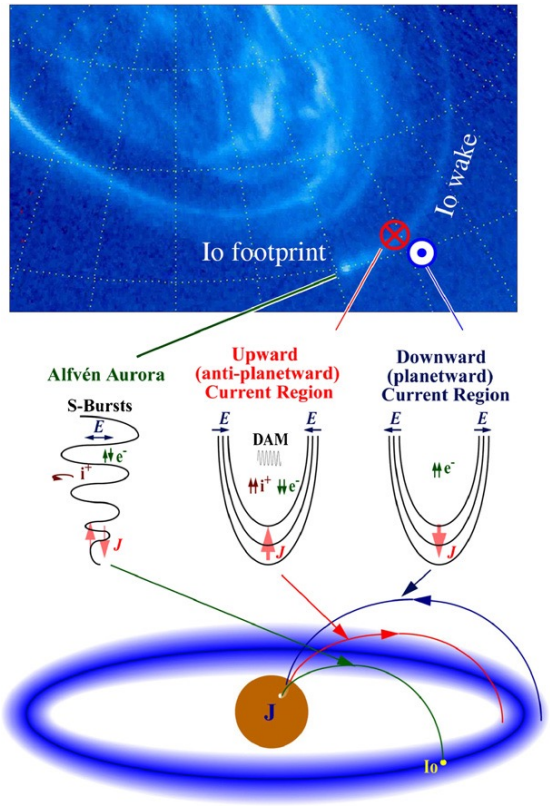

The DAM emissions are associated with currents returning to Io from Jupiter in Io's wake region.

SOURCE: Bagenal (2007).

3 THE SATELLITE EUROPA

Europa is a rocky satellite, covered with ice, orbiting Jupiter at the radial distance of 9.4 R_J in a period of $\sim$ 3.5 earthly days. It is similar to the Earth's moon in size, with a radius of $\sim$ 1560 km. Among the Galilean satellites, Europa is the closest ice-covered moon to Jupiter, followed by Ganymede and Callisto. The presence of water ice on the surface of these satellites was inferred from their densities, albedo and spectral data. From Europa's estimated density and low moment of inertia, it was inferred that the satellite's interior is differentiated, most likely with an outer shell of water ice of about $\sim$150 km thickness, a silicate mantle and a metallic core. The physical state of the entire outer shell, however, could not be defined from those parameters (ANDERSON et al., 1998; SHOWMAN; MALHOTRA, 1999; GREELEY et al., 2004; KRUPP et al., 2010). Some parameters of Europa are found in Table 3.1.

Table 3.1 - Characteristics of Europa.

Radius	$\sim$ 1560 km
Mean Density	$\sim$ 3010 km/m^3
Periodicity	$\sim$ 85.22 h
Distance from Jupiter's center	9.4 R_J ($\sim$ 672,000 km)
Gravity	1.314 m/s^2
Moment of inertia $\left(\frac{C}{MR^2}\right)$	0.346 $\pm$ 0.005
Albedo	0.63

Source: Anderson et al. (1998) and Krupp et al. (2010).

The surface of Europa has very few impact craters, which indicates a relative young age (of no more than a few hundred million years (LISSAUER; PATER, 2013)). Its surface is widely marked by troughs, ridges and bands that appear as lineaments. The ridges are the most common landform on Europa's surface and their formation is usually associated with tension fracturing of the outer layer followed by the upwelling of warm ice or water. This material may be originated from a subsurface water ocean or by heat from the friction between plates of the icy crust, caused by diurnal tidal stresses (PAPPALARDO et al., 1999; GREELEY et al., 2004).

Among the lineaments, the bands are the most easily observed landforms due to their dark color and large width. They are thought to be formed by material from below the surface coming up through the separation of ice plates. For this reason, the

origin of the bands is commonly associated with the formation of the sea floor in the middle ocean ridges at the Earth's surface. Similarly, the dark plains are other widely observed features formed by material originated bellow the surface, however, associated with cryovolcanic activity. The presence of all of these features indicates that Europa may be geologically active. This fact is mainly due to Jupiter's gravitational attraction and to the Laplace resonance[1] with Io and Ganymede (PAPPALARDO et al., 1999; GREELEY et al., 2004; GRASSET et al., 2013).

3.1 An Earth-like ocean on Europa's subsurface

The possible presence of an Earth-like ocean beneath the icy surface of Europa started to be contemplated upon the inference that the outer layer is composed of water ice and upon the models of formation of observed geological features on the surface of the satellite. Besides of having origin associated with the existence of a liquid ocean, the common lineaments on Europa also indicate the nonsynchronous rotation of the surface, which occurs due to the detachment of the outer crust to the interior. This detachment causes the outer crust to rotate in a period slightly different than the interior's rotation period, changing the face of Europa toward Jupiter along its orbits around the planet. As a consequence of that, the direction of the diurnal tidal stress on the surface slowly changes along the years, which can be noticed by comparing the direction of groups of lineaments with different ages. The newer bands are generally darker. The nonsynchronous rotation of the Europa's surface is a strong evidence of the surface liquid ocean since it requires a non-viscous agent separating the icy crust from the rocky interior (PAPPALARDO et al., 1999).

However, the strongest evidence of the liquid water ocean in Europa was detected through Galileo spacecraft's measurements of the magnetic field in Jupiter's magnetosphere. The measurements showed perturbations in the vicinity of Europa that were interpreted as consequences of the effect of an induced magnetic field in the satellite. Analyses of this data indicate that the presence of an ocean with salinity similar to the one of the Earth's ocean, located near the surface of Europa, and with thickness larger than 10 km could generate the observed perturbations (KHURANA et al., 1998; ZIMMER et al., 2000; KHURANA et al., 2009).

The magnetic field induction in the subsurface ocean is set due to the intense variation of Jupiter's magnetic field in the vicinity of the satellites along the rotation of

[1] Laplace resonance or Laplace orbital resonance is the effect in two or three celestial bodies whose orbital periods are in a simple integer ratio. The ratio between the periods of Io, Europa and Ganymede is 1:2:4.

the planet. Jupiter's dipole moment is tilted about 10° with respect to the rotation axis, causing the magnetic equator to sweep up and down over Europa at Jupiter's synodic period. The time-varying component of the jovian magnetic field is mainly radial and drives an induced dipole moment in the equatorial plane of the conductive satellites (NEUBAUER, 1999; KIVELSON et al., 2004; KIVELSON et al., 2009). Figure 3.1 shows a representation of the magnetic induction within a conductive satellite due to the variation of the radial component of Jupiter's magnetic field. Additionally, the B_z component also varies in Europa, but at the satellite's orbital period ($\sim$ 85.22h), because of the eccentricity of its orbit (0.009) (KHURANA et al., 2009).

Figure 3.1 - Schematic representation of the magnetic induction on conductive satellites due to Jupiter's magnetic field variation, in the satellites' rest frame, along the rotation of the planet.

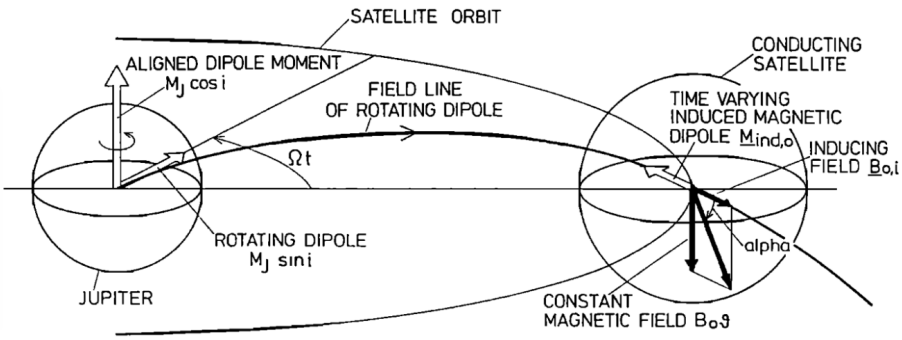

SOURCE: Neubauer (1999).

More recently, the idea of an ocean similar to the Earth's ocean on Europa and the influence of Jupiter's gravitational attraction on the geological activity in the satellite were strengthened by images taken by the Hubble Space Telescope's STIS that show variable concentrations of Hydrogen and Oxygen in the atmosphere of Europa. Persistent enhancements of brightness of the emissions associated with the H and O atoms were observed in a few periods of observation, indicating variable water vapor plume activity occurring on Europa. Besides that, the occurrence of the observed plumes seems to agree with the opening and closing of features on the surface due to the variation of tidal stresses along Europa's orbital period (ROTH et al., 2014).

The presence of the ocean beneath the surface of Europa may affect the electrodynamic interaction between the satellite and Jupiter, mainly because of the variations

in the ambient magnetic field. Therefore, the field induction certainly contributes for the generation of satellite auroral radio emissions on Europa's footprint (KIVELSON et al., 2004).

3.2 Control of the jovian radio emission

The control of the jovian DAM by Europa started to be investigated soon after the identification of Io's control. In order to observe evidences of control by satellites other than Io, Dulk (1967) analyzed DAM emissions from Jupiter detected between 1961 and 1965 by the Boulder spectrographic interferometer. In this analysis, the author made plots of the emissions as a function of the orbital phase of the satellites and Jupiter's CML, which is represented by LCM on the plots. Figure 3.2 shows the non-Io-induced events plotted as a function of Europa's phase (Φ_{Eu}) and the LCM. Each line represents one event. The events related to Io were discarded in order to avoid the effect of this satellite, since its orbital period is half of Europa's period. It can be seen from the plot that no significant concentration of events was observed along the axis of Europa's phase, indicating lack of evidence of control of the jovian DAM emissions by Europa on the observations of the Boulder interferometer.

Figure 3.2 - Non-Io jovian DAM for the period of 1961-1965 from the Boulder interferometer as a function of Europa's phase and Jupiter's CML (LCM).

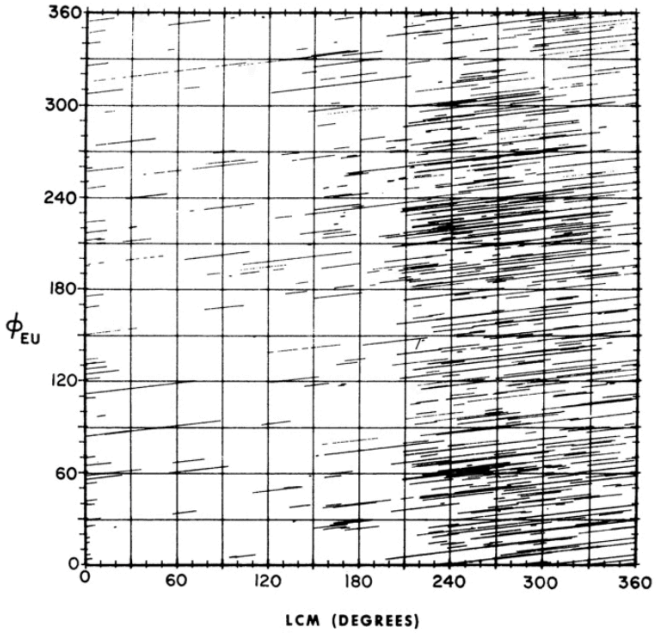

Each line represents one emission.

SOURCE: Dulk (1967).

However, the lack of evidence of the control of the jovian DAM cannot be interpreted as an indication of no control by Europa since it may be the result of the insufficient amount of available samples. Consequently, this strengthens the necessity of extensive catalogs of events to make the detection of control (or not) by satellites other than Io possible and more accurate.

The start of space age and spacecraft observations above the Earth's ionosphere applied to Jupiter's radio emissions enabled the detection of other frequency bands besides the DAM and a more continuous data acquisition, since it does not depend on the Earth's movement. Upon the observation of UV emissions from the footprints of Europa and Ganymede on Jupiter's atmosphere by the STIS (CLARKE et al., 1998; CLARKE et al., 2002), the idea of control of part of the jovian radio emissions by those satellites was enforced and studies of the radio emissions for evidences of control were intensified, mainly with data from spacecraft.

Higgins et al. (2006) analyzed Jupiter's radio emissions in the frequency band of 2.0 – 5.6 MHz from 33 Galileo orbits during 1996 and 2002. From the plot of occurrence probability of those emissions, the authors observed a faint but significant enhancement in the probability of occurrence for Φ_{Eu} between 270° and 300° and CML range of $290° - 320°$, indicating the possible control of part of Jupiter DAM by Europa. The plot is presented in Figure 3.3, where the green color represents the highest probability observed. This indication observed by Higgins et al. (2006) was confirmed by the analysis of jovian emissions with frequencies between 2.1 and 5.8 MHz from data obtained during the flybys of Voyager 1 and 2 around Europa (HIGGINS, 2007). From plots of occurrence probability of these emissions versus Europa's phases and Jupiter's CML, Higgins (2007) observed enhancements of occurrence probability in $250° \leq \Phi_{Eu} \leq 280°$ and $85° \leq \Phi_{Eu} \leq 115°$ ranges, both in CML from 290° to 350°.

More recently, in order to improve the identification of emissions induced by Europa on spacecraft data catalogs, Louis et al. (2017) used the ExPRES (Exoplanetary and Planetary Radio Emissions Simulator) to predict the dynamic spectra of Europa-related emissions and to compare the predictions with the data from Voyager 1, 2 and Cassini. The emissions identified through the comparison between the real data and the simulated data were selected and plotted as a function of Φ_{Eu} and Jupiter's CML. The plots are presented in Figure 3.4, showing two regions in Φ_{Eu} of accumulation of emissions: $\sim 100°$ and $\sim 260°$. Furthermore, the emissions were also counted and characterized with regard to their source, minimum and maximum frequencies and duration. Some of those characteristics will be discussed in a comparison to our

results in Chapter 7.

Other catalog of jovian emissions that has already enabled the detection of the control by the Galilean satellites other than Io is the NDA's catalog. The NDA is located at Nançay, in central France, and observes Jupiter daily for nearly 8 hour/day (BOISCHOT et al., 1980; MARQUES et al., 2017). Although the jovian radio emissions detected by ground-based instruments are not as continuous as the emissions detected by spacecraft, the long term daily observations may collect an amount of events equivalent to the spacecraft's in addition to provide information about the long term behaviour of the emissions.

Figure 3.3 - Occurrence probability of Jupiter's DAM emissions from 1996 to 2002 plotted as a function of Jupiter's CML and Φ_{Eu}.

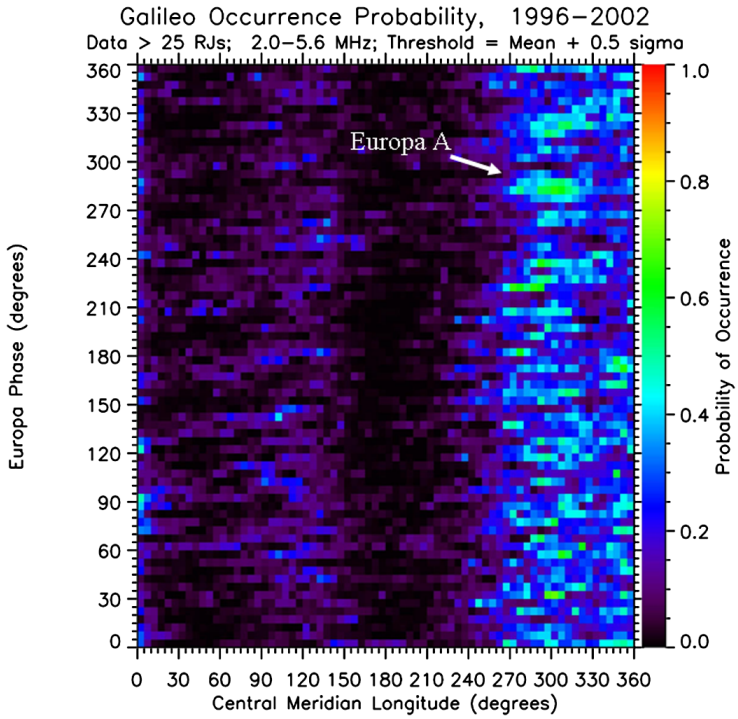

Data from the Galileo spacecraft.
SOURCE: Higgins et al. (2006).

Using that long term database, Zarka et al. (2017) analyzed the NDA's catalog, at that time with 26 years of observation, in order to identify possible control of jovian DAM emissions by Ganymede, Europa, Callisto and Amalthea. For Europa, the events considered for analysis were those independent of both Io and Ganymede

(non-Io and non-Ga DAM), according to their results obtained for the Ga-DAM and to previous studies for the Io-DAM (MARQUES et al., 2017). The occurrence probability of those events was calculated from the numbers of emissions and of observations occurring in each $5° \times 5°$ box on the CML$\times\Phi_{Eu}$ plane. The probabilities were separately plotted by the hemisphere of origin of the events, as shown in Figure 3.5.

Figure 3.4 - Jovian Eu-DAM emissions detected on the Cassini's and the Voyagers' data catalogs, by comparison with simulated dynamic spectra, plotted as a function of Φ_{Eu} and Jupiter's CML.

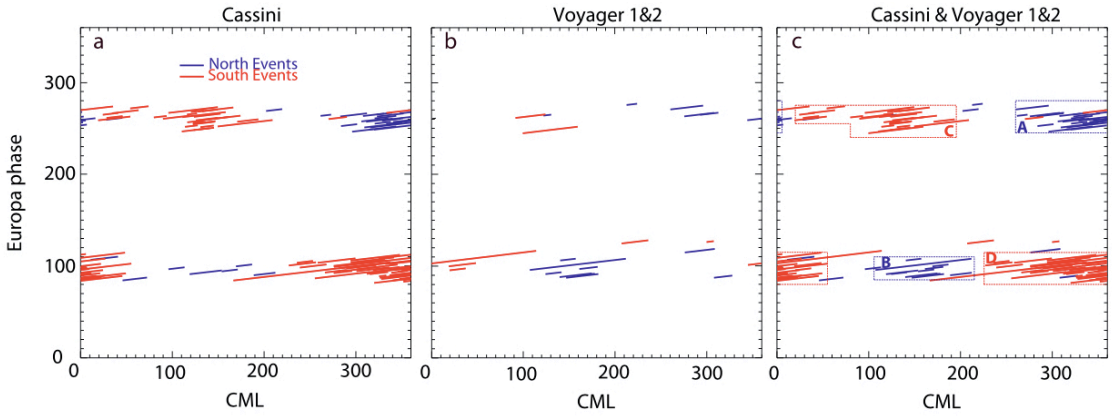

The distinction between North events or South events refers to the hemisphere of origin of the emissions, which is inferred from the emissions' sense of polarization. The capital letters A, B, C and D indicate the emissions' probable sources on Jupiter.

SOURCE: Louis et al. (2017).

In Figure 3.5, the plots *a* and *c* are related to the emissions from the Northern hemisphere; and the plots *b*, *d* and *e*, to the emissions from the Southern hemisphere. For the northern hemisphere, most of the emissions occurred in CML ranging from $200° - 285°$, and a strong modulation of the occurrence in the Φ_{Eu}'s axis is observed, with peaks at $\Phi_{Eu} \simeq 50°$ and $\Phi_{Eu} = 250°$. For the southern hemisphere, most of the emission occurrence is gathered in the CML range of $290° - 30°$ (or $290° - 390°$, as it is shown in plot *e*), where a strong peak of occurrence probability was observed in $\Phi_{Eu} \simeq 260°$. Furthermore, another peak was also observed in $\Phi_{Eu} = 130°$, within the CML range of $200° - 285°$ (ZARKA et al., 2017).

Figure 3.5 - Occurrence probability of jovian non-Io and non-Ga emissions from the NDA's catalog (1990 to 2015).

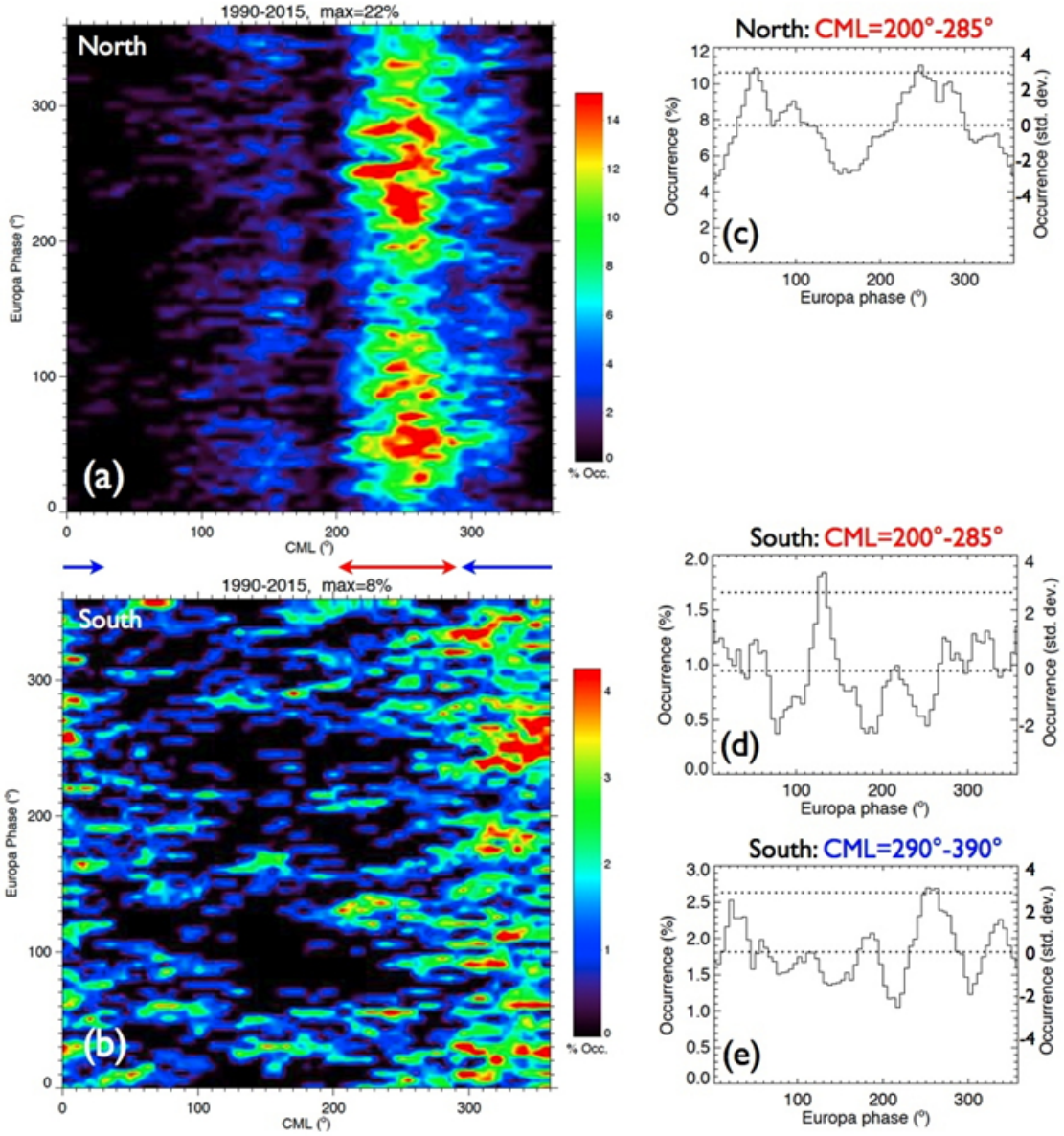

SOURCE: Zarka et al. (2017).

4 CYCLOTRON MASER INSTABILITY

The Cyclotron Maser Instability (CMI) is the main generation mechanism of the known planetary auroral emissions. The CMI is a consequence of the resonance between electrons gyrating along magnetic field lines and elliptically polarized electromagnetic waves generated by perturbations in the plasma. The resonance occurs when the electric field of the wave is in phase with the electrons in cyclotron motion and enables withdraw of free energy in the electric distribution by the wave, causing its amplification (DULK, 1985; ZARKA, 1998; MARQUES et al., 2017).

Because of the resonant character of the CMI, the emissions resulting from it are the so-called "coherent" emissions. The "incoherent" emissions, on the other hand, result from acceleration of individual electrons by collision or by a magnetic field. The bremsstrahlung and the gyrosynchrotron radiation correspond to "incoherent" emissions (DULK, 1985).

The following presentation of the theoretical deduction of the CMI is based on the works of Wu et al. (1973), Wu and Lee (1979), Wu (1985), Dulk (1985), Zarka (1998), Galopeau et al. (2004), Parks (2004), Hess et al. (2008) and Marques (2017).

4.1 Theoretical deduction

In order to deduce the CMI, we will consider a homogeneous plasma in a uniform magnetic field $\vec{B}_0$ ($\hat{b} \parallel \hat{z}$), and perturbation waves proportional to $\exp^{i(\vec{k}\cdot\vec{x}-\omega t)}$, where $\vec{k}$ is the wave vector and ω, is the angular wave frequency. Furthermore, we limit the analysis to the regions in which the electron cyclotron frequency is much higher than the plasma frequency ($\omega_{pe}/\omega_{ce} \ll 1$, $\omega_{pe} = [ne^2/(m\epsilon_0)]^{1/2}$ and $\omega_{ce} = eB/m$, where e and m are, respectively, the charge and the mass of the electron; B, is the local magnetic field and n, the electron density). The instability occurs when the wave's frequency is similar to the local electron cyclotron frequency ($\omega \simeq \omega_{ce}$), configuring resonance between the wave and the electrons in cyclotron motion. In those conditions, the wave's growth rate for the ordinary mode is smaller than the growth rate for the extraordinary mode (WU, 1985), which explains the total circular or elliptical polarization of the jovian DAM (ZARKA, 1998; CLARKE et al., 2004).

The electric field of the perturbation may be described as:

$$E_{\pm} = E_x \pm iE_y$$

$$E_{||} = E_z$$

with E_+ and E_- denoting the electric field circularly polarized in the left hand (LH) sense and in the right hand (RH) sense, respectively. The electric field of the perturbation can be found by:

$$D(\vec{k},\omega)\cdot\begin{bmatrix}E_+\\E_-\\E_{||}\end{bmatrix} = \begin{bmatrix}0\\0\\0\end{bmatrix} \tag{4.1}$$

where

$$D(\vec{k},\omega) = \begin{bmatrix}\frac{k}{2}-\frac{i\mu_o\omega}{4}J_+ & \frac{k}{2}-\frac{i\mu_o\omega}{4}J_- & i\mu_o c^2 k_\perp R\\ \frac{k}{2i}-\frac{\mu_o\omega}{4}J_+ & -\frac{k}{2i}+\frac{\mu_o\omega}{4}J_- & 0\\ 0 & 0 & K+i\mu_o c^2 k_{||}R - i\mu_o\omega J_{||}\end{bmatrix} \tag{4.2}$$

with

$$K = \left(k^2 - \frac{\omega^2}{c^2}\right),$$

$$R = \frac{e^2}{2i\pi}\iint_D \frac{\partial f/\partial p}{\gamma m\omega - k_{||}p_{||}}\gamma m p_\perp dp_{||}dp_\perp,$$

$$J_\pm = \frac{e^2}{2i\pi}\iint_D \frac{\partial f/\partial p_\perp}{\gamma m\omega - k_{||}p_{||} \pm m\omega_c}p_{||}p_\perp dp_{||}dp_\perp,$$

$$J_{||} = \frac{e^2}{2i\pi}\iint_D \frac{\partial f/\partial p_{||}}{\gamma m\omega - k_{||}p_{||}}p_{||}p_\perp dp_{||}dp_\perp.$$

where $f = f(v)$ is the electron velocity distribution function; p stands for electron's momentum; γ, for the Lorentz factor; and the integration domain is $D = \{(p_{||}, p_\perp) \in \mathbf{R}\times\mathbf{R}_+\}$.

4.1.1 Resonance condition

The condition for resonance is taken from the dispersion relation of the perturbation wave, which is obtained by considering the determinant of the matrix $D(\vec{k},\omega)$ (Equation 4.2) equal to zero. For the RH component, we have $E_+ = E_{||} = 0$. Then, the dispersion relation is:

$$k^2 - \frac{\omega^2}{c^2} - \frac{\mu_0 e^2 \omega}{4\pi m} \iint_D \frac{\partial f/\partial v_\perp}{\omega - k_{||} v_{||} - \omega_c/\gamma} v_\perp^2 dv_{||} dv_\perp = 0 \tag{4.3}$$

From Equation 4.3, the resonance condition is:

$$\omega - k_{||} v_{||} - \omega_c/\gamma = 0 \tag{4.4}$$

Applying the Lorentz factor approximation ($\gamma^{-1} = 1 - v^2/2c^2$, where $v^2 = v_\perp^2 + v_{||}^2$) to Equation 4.4 for a weak relativistic approximation:

$$\omega - k_{||} v_{||} = \omega_c \left(1 - \frac{v^2}{2c^2}\right) \tag{4.5}$$

$$\left(v_{||} - \frac{c^2 k_{||}}{\omega_c}\right)^2 + v_\perp^2 = 2c^2 - \frac{2c^2\omega}{\omega_c} + \frac{c^4 k_{||}^2}{\omega_c^2} \tag{4.6}$$

Equation 4.6 is a circle equation in the plane $(v_{||}, v_\perp)$, with center in $v_{||o}$ and radius R:

$$\left(v_{||} - v_{||o}\right)^2 + v_\perp^2 = R^2 \tag{4.7}$$

$$v_{||o} = \frac{c^2 k_{||}}{\omega_c} \tag{4.8}$$

$$R^2 = 2c^2 - \frac{2c^2\omega}{\omega_c} + v_{||o}^2 \tag{4.9}$$

The circle of resonance is represented in Figure 4.1 for the loss-cone and the shell electron distributions.

4.1.2 Growth rate

In the particle-wave interaction, the wave damping or growing is indicated by the growth rate (ω_i) in the complex frequency ($\omega = \omega_r + i\omega_i$, $|\omega_i| \ll \omega_r$). The wave is amplified when $\omega_i > 0$. The growth rate is derived from the wave dispersion equation by applying the Plemelj's formula. From the dispersion equation for the RH polarized component (Equation 4.3), we have (WU; LEE, 1979):

$$\omega_i = \frac{\omega_p}{8} \int_0^{+\infty} v_\perp^2 dv_\perp \int_{-\infty}^{+\infty} \frac{\partial f}{\partial v_\perp} \delta \left(\omega_r - k_{||} v_{||} - \frac{\omega_c}{\gamma} \right) dv_{||} \tag{4.10}$$

where $f = f(v)$, and δ is the Dirac delta function. From Equation 4.10, we have that $\omega_i \propto \partial f / \partial v_\perp$. Therefore, the instability occurs when $\partial f / \partial v_\perp$ is positive. Figure 4.1 shows sketches of a loss-cone distribution (a) and a shell distribution (b), with the CMI resonance circle. The regions of positive $\partial f / \partial v_\perp$ are indicated by the red arrows. In the shell distribution, $v_{||o} = 0$ and the $\partial f / \partial v_\perp > 0$ occurs on the shell's inner border (GALOPEAU et al., 2004; HESS et al., 2008).

Figure 4.1 - Sketches of the circle of resonance for the loss-cone and the shell electron distributions.

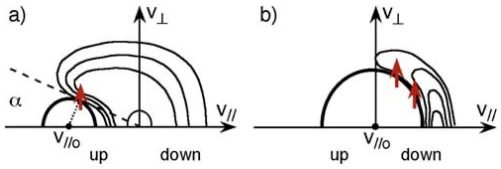

(a) The loss-cone distribution. α is the pitch angle, and the red arrow indicates the largest positive $\frac{\partial f}{\partial v_\perp}$. (b) The shell distribution. $\frac{\partial f}{\partial v_\perp}$ is positive on the shell's inner border.

SOURCE: Hess et al. (2008).

4.1.3 Dependence on the magnetic field's vector direction

In Equation 4.8, by considering $k_{||} = \frac{\omega}{c}(\hat{k} \cdot \hat{b})$, where $\hat{b}$ is the magnetic field's versor, and $\omega \simeq \omega_c$, we have:

$$v_{||o} = \frac{c^2 \omega}{\omega_c c} (\hat{k} \cdot \hat{b}) \simeq c. \cos(\theta) \tag{4.11}$$

Equation 4.11 shows the dependence of the instability on the magnetic field direction, since the angle between the wave's propagation direction and the magnetic field vector (θ) must be less than $\pi/2$ for $v_{||o}$ to be positive. The same dependence is also observed when we consider the component with LH polarization, which has a stronger interaction with the electron population in cyclotron motion when $\vec{k}$ and $\hat{b}$ are anti-parallel. In this case, the resonance condition is:

$$\omega - k_{||} v_{||} + \omega_c/\gamma = 0 \tag{4.12}$$

From which we have:

$$v_{||o} = -\frac{c^2 k_{||}}{\omega_c} \simeq -c.\cos(\theta) \tag{4.13}$$

Therefore, the hemisphere of origin of the emissions may be inferred from the sense of the wave's dominant polarization.

4.1.4 Beaming angle

Because of the symmetry around the magnetic field line, θ is the mid-aperture angle of the CMI beaming cone. An equation for θ was determined by Hess et al. (2008) by applying Equation 4.11 to the loss-cone distribution. Satellite observations of the region source of the Earth's AKR have indicated that the energy for the CMI comes most probably from the loss cone distribution (WU; LEE, 1979). Moreover, Juno's in situ plasma, wave and magnetic field observations analyzed for the jovian HOM emission also suggested that the CMI on Jupiter may be driven by the loss-cone distribution as well as on Earth (LOUARN et al., 2017). Therefore, since the jovian non-Io-DAM and HOM may be the same radio component emitted in different latitudes (ZARKA, 1998; ECHER et al., 2010), it may be supposed that the loss-cone distribution provides enough energy for the jovian DAM.

From Hess et al. (2008):

$$v_{||o} = \frac{v}{\cos\alpha} \tag{4.14}$$

where α is the loss-cone angle:

$$\alpha = \arcsin\left(\sqrt{\frac{B_o}{B_m}}\right) = \arcsin\left(\sqrt{\frac{\omega_c}{\omega_{c,max}}}\right) \tag{4.15}$$

where B_o and ω_c are, respectively, the magnetic field and electron cyclotron frequency at the equatorial plane; and B_m and $\omega_{c,max}$, the maximum magnetic field and electron cyclotron frequency, at the mirroring point.

Then, the aperture mid-angle of the beaming cone is given by:

$$\theta = \arccos\left(\frac{v}{c}\left(1 - \frac{\omega}{\omega_{c,max}}\right)^{-1/2}\right) \tag{4.16}$$

where ω is the wave's frequency and $\omega_{c,max}$, the cyclotron frequency at Jupiter's ionosphere. From Equation 4.16, it is inferred that the beaming angle is inversely proportional to the wave's frequency. Therefore, the wave emission occurs in different coaxial beaming cones, with the highest frequency waves being emitted at the most internal cone.

5 INSTRUMENTATION

In this chapter, the limitations of the observations of the emissions and the angles that characterize the observations will be discussed. The major observation limitations result from the beaming conditions and the rotation of Jupiter and the Earth; and the angles concern to the orbital position of the satellites and the longitude of the observer-Jupiter line with respect to the jovian CML. These parameters are also considered for the classification of the emissions' possible source. Besides that, the data catalog analyzed in this work as well as the instrumentation responsible for its acquisition are also presented.

5.1 Geometry of the observations

Resulting from the CMI, radio emissions are detected by spacecraft and/or ground-based instruments, depending on the emissions' frequency and the cut-off frequency of the Earth's ionosphere. In both cases, the emissions are detected when the walls of the beaming cone points to the observer. For a fixed observer, looking at Jupiter's dayside, the emissions are detected only when the beaming cones are centered on the dawn or dusk limbs of Jupiter. It occurs due to the high values of θ, which are up to $70° - 80°$ (QUEINNEC; ZARKA, 1998; HESS et al., 2008). Thus, there are four sources of satellite DAM emissions on Jupiter. Two in each hemisphere: A and B in the North, and C and D in the South (HESS et al., 2012; MARQUES et al., 2017). Figure 5.1 presents the sources and their position in Jupiter's hemispheres and sides at the reference frame of an observer located out of figure plane.

Figure 5.1 also presents the arc patterns of the emissions on the dynamic spectra (*time* $\times$ *frequency* plane). The arcs result from the rotation of the multiple coaxial beaming cones with Jupiter's magnetic field lines (from left to the right in the figure). At the B and D sources (dawn side), the most external cone points first to the observer and is followed by the more internal cones. Therefore, the detected frequencies increase with time, forming the so-called Vertex Early arc. The beaming cones continue to rotate with Jupiter and their emissions stop being observed until they reach the dusk side. There, at the A and C sources, the most internal cone points first to the observer and is followed by the more external cones. Therefore, the detected frequencies decrease with time, forming the so-called Vertex Late arc (HESS et al., 2012).

The source of the observed emissions may be then inferred from the sense of dominant polarization of the emissions, which indicates their hemisphere of origin (RH

for the Northern hemisphere and LH for the Southern hemisphere) and the shape of the formed arc on the dynamic spectra. Besides that, the sources in the same hemisphere may also be differentiated from the values of longitude of the observer-Jupiter line associated with the emissions (MARQUES et al., 2017). This longitude is indicated on the plots in the so-called CML axis. Due to the geometry of the observation, there are some "active" ranges of CML, which are not exactly the same in each hemisphere. The emissions from the A source are related to the CML of $\sim 240°$; B and D, to $\sim 150°$; and C, to $\sim 320°$. Although B and D sources have the same average CML, the range associated with the occurrence of their emissions is not the same (HESS et al., 2012; MARQUES et al., 2017). This is clearly observed in Figure 5.2, where the distribution of jovian non-Io DAM emissions along the entire CML range and Io's phase angle (Φ_{Io}) is shown in different colors. Each color represents one emission source on Jupiter.

Figure 5.1 - Representation of the beaming cones at Jupiter in their positions from where the emissions may be detected by an observer.

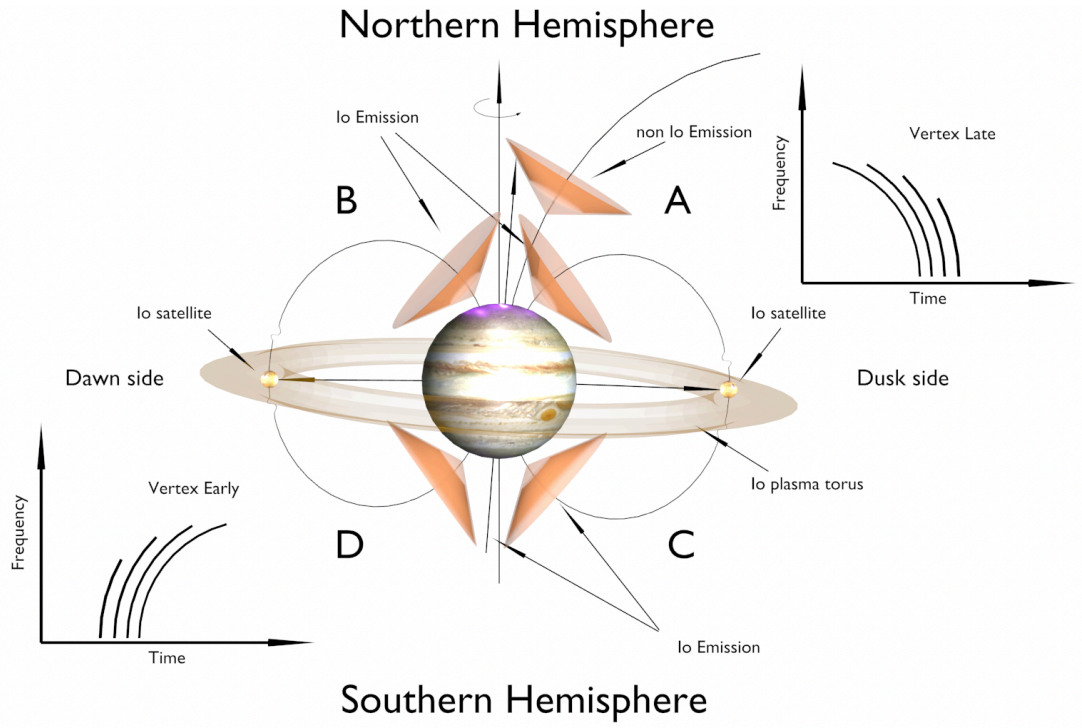

The position of the cones is given with regard to the observer-Jupiter line, with the observer located out of the page. The emissions may be detected only when they are originated at the limbs of Jupiter, due to the high values of θ. The arcs on the f-t diagrams represent the pattern arcs formed by the Io-DAM emissions when detected by the observer.

SOURCE: Marques et al. (2017).

Figure 5.2 - Non-Io DAM emissions on the NDA's catalog plotted as a function of Φ_{Eu} and Jupiter's CML.

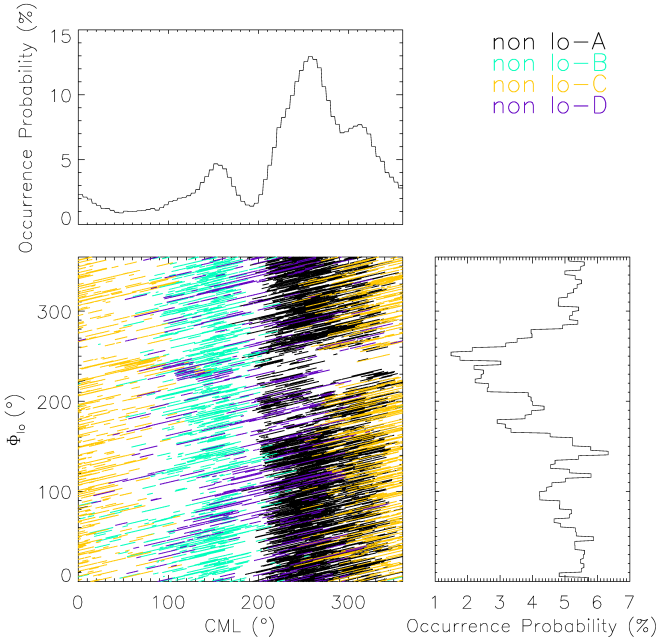

The emissions are represented by the lines on the plot. The different colors indicate the emissions' source on Jupiter (A, B, C or D). The emissions from the same source are related to a specific range of CML when detected by the same observer.

SOURCE: Marques et al. (2017).

For better comprehension of the data analysis performed in this work, it is important to consider how the angles which characterize the geometry of the observations are counted and what they represent. These angles indicate the position of components of the emission system, as the satellites and the active field line, given with respect of the observer position (the phase angles) and of Jupiter's central meridian (the longitudes). The phase angle (Φ) is counted counterclockwise from the opposition to the observer, as it is indicated for Io by the blue narrow in Figure 5.3. The longitudes (Λ and CML) are calculated from the jovian central meridian, which was set as being the position of the Earth-Jupiter line at 00h00m00s on January 1st 1965 (MEILLER, 1980). This was established due to the fact that Jupiter is a gas planet, not having a fixed point on its surface to mark a stated central meridian. Then, the longitudes are counted as a function of Jupiter's rotation period (of 9h55m29.711s) (HIGGINS et al., 1997; BAGENAL et al., 2017). In Figure 5.3, the central meridian of Jupiter is indicated by the straight green line and the green arrow so-called CML indicates the longitude counting sense.

In Figure 5.3, Φ_a and Λ_a are, respectively, the phase and longitude of the active field line; Φ_{Io} and Λ_{Io}, the phase and longitude of Io; and δ_a is the lead angle, which is the phase difference between the active field line and Io in the instant of the emission (HESS et al., 2008; MARQUES, 2017). Each jovian DAM emission analyzed in this work is associated with corresponding values of the observer's longitude (CML) and of the phase angles of the Galilean satellites and Amalthea, making it possible to plot the emissions (or their occurrence probability) as a function of any of those parameters.

Figure 5.3 - Sketch of all the angles that represent the orbital location of Jupiter's satellites, active field line and the observer-Jupiter line.

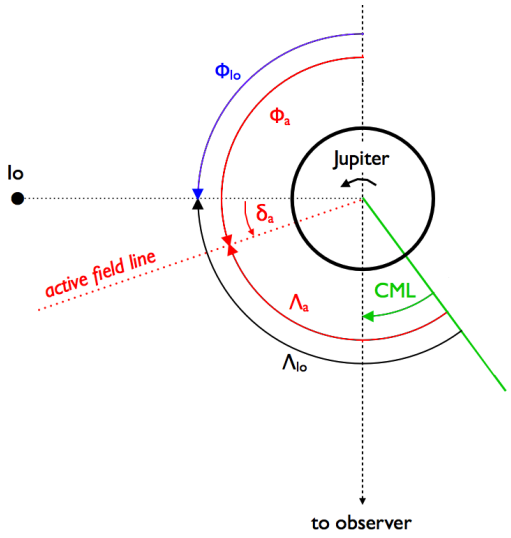

Φ_a and Φ_{Io} are the active field line's and Io's phase angles, respectively; Λ_a and Λ_{Io} are the active field line's and Io's longitudes, respectively. The angles for Io may be applied to any other jovian satellite. δ_a is the lead angle; CML stands for the Central Meridian Longitude of Jupiter, considered in the counting of all the longitudes and represented by the green straight line. The CML angles are the longitudes of the observer-Jupiter line regarding the central meridian, as indicated by the green arrow.

SOURCE: Marques et al. (2017).

The distribution of the emissions' occurrence probability on the CML$\times\Phi_{Sat}$ plane gives information about the control of the emissions by the satellite, as it was discussed through the presentation of previous studies regarding the control of the jovian DAM by Europa, in Chapter 3. The satellite control of the emissions is indicated by regions of high probability of emissions' occurrence in specific ranges of the satellite's phase and CML. Those regions suggest the existence of favorable longi-

tudes of Jupiter for emissions occurrence and detection, and the emissions induction by field-aligned currents in the satellite's wake region, due to the longitudinal proximity of the satellite to the emission's source (as discussed in Section 2.3). On the other hand, the uniform distribution of emissions' occurrence probability along the satellite's phase indicates that the observed emissions occur regardless of the satellite position in its orbit, and, therefore, do not point to satellite control.

Also, because of the expected proximity of the satellite to the emissions' source for satellite-driven emission induction, the satellite's orbital phase is another parameter considered for the classification of the emissions' possible sources. The sources A and C (dusk side) are usually associated with $\Phi_{Sat} =\sim 250°$, while the sources B and D (dawn side), to $\Phi_{Sat} =\sim 100°$, with slight variations (LOUIS et al., 2017; MARQUES et al., 2017; ZARKA et al., 2018).

5.2 Nançay decameter array

The Nançay Decameter Array (NDA) is a phased array located in the Station of Radioastronomy of Nançay, France. It was built in the 1970s for the study of decametric radio emissions from the Sun and Jupiter, becoming operational in late 1977. The NDA is sensible to the frequency range of 10 MHz – 120 MHz, making it possible to detect most part of the frequency range of Jupiter DAM emissions from the ground. Before the 1970s, other arrays had already been observing these powerful radio sources. Nevertheless, the NDA was built in order to improve the observation of the radio emissions by providing qualities that were not seen together in any array before: wide bandwidth; high time and frequency resolution; high sensitivity; and long tracking time (BOISCHOT et al., 1980). Figure 5.4 shows the antennas that compose the array.

The antennas of the NDA are simultaneously connected to different receivers, are separated in sub-arrays with circular polarization in opposite senses and are distributed over a physical area of 7000 m^2. Those features ensure that the observations may be presented in different resolutions, that the array has a high sensitivity, and that it can detect all circular or elliptical polarized emissions (BOISCHOT et al., 1980; LAMY et al., 2017).

5.2.1 Antennas and receivers

The NDA consists of 144 conical helical antennas of 9 meters high, with a diameter of 5 meters at the base, and inclined by 20° S in the meridian plane to increase

the gain in that direction. The antennas have eight copper-coated steel wires on their superficial area. Six wires are connected to diode switches, and the other two, which are diametrically opposite, are left disconnected. The connection of the wires configures the phase of the antenna, which changes by $\pi/4$ in each variation through the diode switches (BOISCHOT et al., 1980; LECACHEUX, 2000; LAMY et al., 2017). Figure 5.5 presents a model of the NDA's antennas.

Figure 5.4 - The Nançay decameter array.

SOURCE: Radioastronomy Station of Nançay (2020).

The array is divided in two sub-arrays with 72 antennas each: one circularly polarized in the right-hand circular sense, and the other, in the left-hand circular sense. Besides that, the antennas in the sub-arrays are separated by their phases, which are determined by rotation and by delay-lines (AUBIER et al., 1975; LECACHEUX, 2000). The different phases of the antennas are important to direct the maximum sensitivity of the array to a specific point in the sky by compensating delays in time due to the point's direction inclination (BOISCHOT et al., 1980; LECACHEUX, 2000; MARQUES et al., 2017).

The NDA has always been simultaneously connected to more than one receiver in order to have the observations in different time and spectral resolutions (BOISCHOT et al., 1980). The receivers are spectral analysers, which were analog until 1990, when digital receivers started being developed and connected to the antennas of the NDA. Recently, the NDA has been connected to four different digital receivers: Routine, New Routine, Mefisto, and JunoN. The data analyzed in this work comes from the Routine, which is the oldest receiver still connected. It has been connected since

1990, measuring the flux density of the emissions polarized in both LH and RH senses at time-frequency resolutions of 500 ms × 75 kHz, for Jupiter, and 500 ms × 175 kHz, for the Sun (LAMY et al., 2017). General information of the Routine receiver is presented in Table 5.1. RR and LL in the table indicate autocorrelation on the RH array and on the LH array, respectively.

Figure 5.5 - The model of the NDA's antennas.

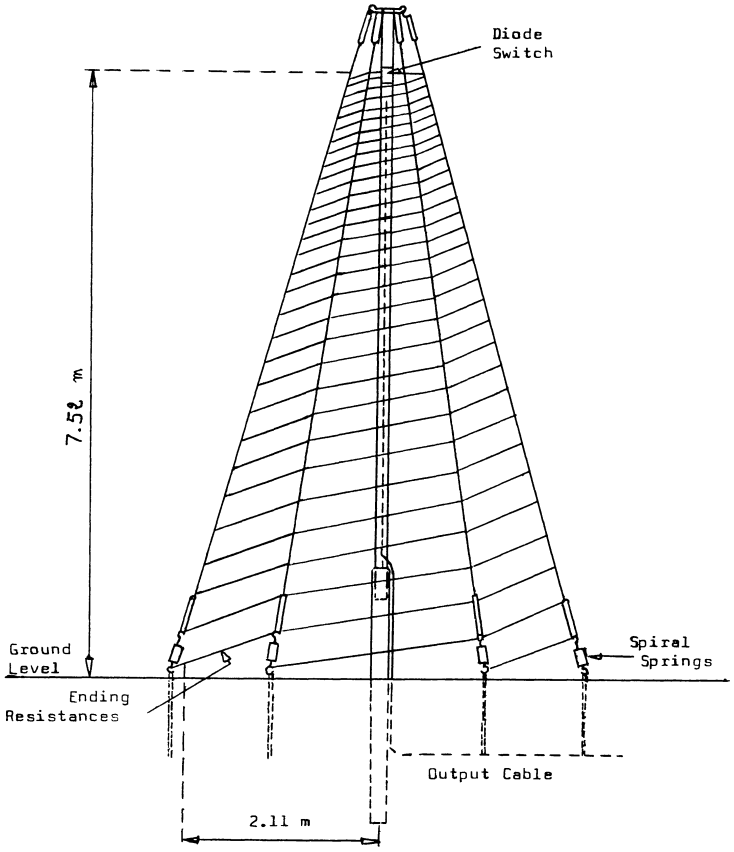

SOURCE: Aubier et al. (1975).

Table 5.1 - Information about the Routine receiver.

Receiver	Measurements	Channels	Spectral Range (MHz)	Resolution (ms×kHz)	Data Volume (per 8h)
Routine (1990-...)	RR,LL	2	10–40 (Jupiter) 10–80 (Sun)	500×75 500×175	22 MB

Source: Lamy et al. (2017).

5.3 Data catalog

The radio emissions detected by the NDA may be observed in dynamic spectra, two for each daily observation of Jupiter: one for each sense of circular polarization. The dynamic spectra present the temporal behaviour (frequency and intensity) of the emissions detected by the Array. Each event (or emission) is actually a package of L-bursts (the roughly vertical thin lines on the diagrams) that appear together. Then, the arcs Vertex early and Vertex late, presented in Section 5.1, are actually formed by the disposition of the L-bursts. In one daily observation of Jupiter by the NDA, none, one or more than one emission may be detected. Figure 5.6 presents two dynamic spectra with three examples of jovian DAM emissions. The observed emissions are induced by Io and were detected by the NDA on 7 August 1999. The intensity of the emissions is indicated in the $f \times t$ diagram by the intensity of the color, as it is shown in the color bar, in dB (MARQUES et al., 2017).

Figure 5.6 - Dynamic spectra showing three Io-DAM emissions detected on 7 August 1999 by the NDA.

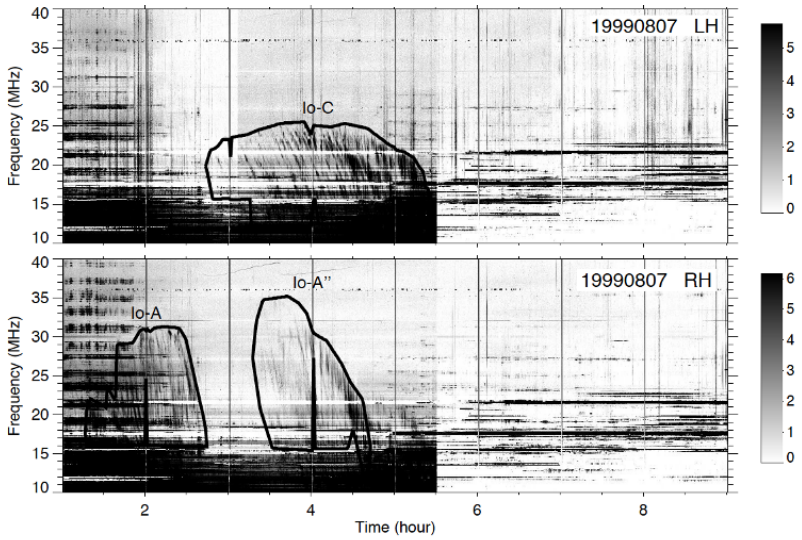

The emissions are represented in the dynamic spectra by the black contours, which comprise several L-bursts. The upper diagram shows an emission with dominant left-hand polarization, induced by Io and originated on the C source. The bottom diagram shows two emissions with dominant right-hand polarization, also induced by Io, and originated on the sources A and A". The apostrophes in the source designation are used to differentiate sources whose emissions appear in CML and/or Φ_{Sat} ranges close but different to the ones of the emissions from the usual sources A, B, C and D.

SOURCE: Marques et al. (2017).

Before 1990, the dynamic spectra were printed in paper of 35 mm films. The digitization of the dynamic spectra by the connection of digital receivers since 1990 made it possible to build a digital database of the observations. The NDA's digital catalog comprises all the daily observations of Jupiter by the Array through the Routine receiver and the emissions visually detected on the dynamic spectra. The emissions are catalogued with their observed characteristics and the corresponding ephemeris data (as the longitude of the Earth-Jupiter line, the phase and the longitude of the Galilean satellites and of Amalthea, and the Sun's and the Earth's jovicentric latitude). The characteristics of the emissions include the start and end times of the emissions' visualization by the array; their duration, which corresponds to these times' difference; their dominant polarization; their intensity and their frequency (MARQUES et al., 2017). Each emission has only one value for intensity on the catalog, which corresponds to its average intensity, calculated after removing the background intensity. On the other hand, with regard to their frequency, the emissions on the catalog are associated with several values of frequency, which correspond to the maximum and minimum frequencies of the observed L-bursts. Therefore, the values of maximum frequency that will be analyzed in this work refer actually to the highest frequency of each L-bursts package. The Doppler effect in the frequencies due to the movement of the emissions' sources and of the Earth is excluded. The current catalog consists of the digital data of 29 years of observations, from 1990 to 2018. This catalog was first compiled by Marques et al. (2017) and is constantly being updated.

6 DATA PROCESSING

In this chapter, the data processing and analysis of the jovian DAM radio emissions on the Nançay decameter array's catalog are described. The results and conclusions of the analysis will be presented in the Chapters 7 and 8.

In order to observe the possible control of part of the jovian DAM by Europa, we selected from the NDA's catalog the emissions not induced by Io neither by Ganymede (non-Io and non-Ga). This procedure was adopted to exclude the effect of these satellites on the emissions and, consequently, due to the satellites' period resonance, to facilitate the detection of the control of part of the jovian DAM radio emissions by Europa. Following Zarka et al. (2017) and Marques et al. (2017), we also separated the non-Io and non-Ga DAM emissions by their hemisphere of origin, according to their dominant polarization, to make it possible to compare the control in each hemisphere and to simplify the determination of the sources (A, B, C or D) on Jupiter.

Then, the occurrence probability of the selected emissions was calculated from the numbers of northern and southern emissions and of observations occurring in each $5° \times 5°$ box on the CML$\times\Phi_{Eu}$ plane, as did Zarka et al. (2017). Figure 6.1 shows the plots with the occurrence probabilities of the emissions from the Northern hemisphere (NH) (plot *a*) and of the ones from the Southern hemisphere (SH) (plot *b*). The control by the satellite is indicated by non-uniform distributions of the probability along the satellite's phase and the CML axes.

From Figure 6.1, we can see that the probabilities for the NH are higher (maximum of 23%) than for the SH (maximum of 10%). This predominance of the RH emissions over the LH emissions is observed for all types of jovian DAM. It is probably related to the higher intensity and stronger gradients of magnetic field at the flux tubes' footprints in the NH in comparison to those in the SH (ZARKA et al., 1996; HESS et al., 2011; MARQUES et al., 2017; CONNERNEY et al., 2018). Moreover, the emission occurrence concentrate in the CML interval of $200° - 285°$ in the Northern hemisphere, while it occurs preferentially in the CML interval of $290° - 40°$ for the Southern hemisphere. These intervals correspond approximately to the values of CML related to the A and C sources, respectively (MARQUES et al., 2017). For both hemispheres, the non-uniform distribution of the red regions (highest probability) along the phase axis suggests control by the satellite Europa.

Figure 6.1 - Occurrence probability of the non-Io and non-Ga emissions on the NDA's catalog plotted as a function of CML and Europa's phase.

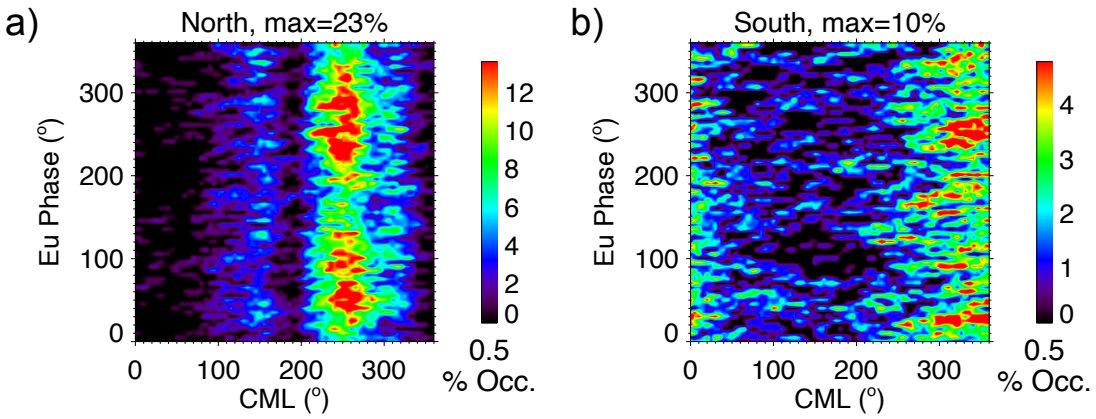

Occurrence probability of the emissions with dominant polarization in the right-hand (RH) sense (a) and in the left-hand (LH) sense (b). Each bin has a resolution of $5° \times 5°$.

SOURCE: Author's production.

For a better evaluation of these distributions, the occurrence probabilities were plotted as a function of Φ_{Eu} in different intervals of CML for each hemisphere. Thus, the peaks were more easily compared. The selection of the CML intervals considered in this analysis was made visually and also following the intervals considered by Zarka et al. (2017) in their study. Figure 6.2 shows the plots related to the CML ranges of $200° - 285°$, $90° - 195°$ and $290° - 340°$ for the Northern hemisphere. The emissions' occurrence probability for each CML range was calculated as before, but taking into account only the emissions with start and end within the contemplated CML interval. For each interval, the mean occurrence probability was calculated and was reduced from the value of probability in each $5°$ bin of Φ_{Eu}. Thus, the result was plotted as a function of the respective occurrence probability standard deviation (σ). The values of σ were separately calculated for each interval of CML and are, therefore, distinct in each plot.

From the plots in Figure 6.2, it may be noted that the occurrence probability within the CML interval of $200° - 285°$ (b) is not uniform along the Europa's phase, being higher in the phase range of $\sim 220° - 310°$ than in $\sim 50° - 150°$. The other plots (c and d), corresponding to CML ranges with less occurrence of emissions, show that the occurrence probability has a roughly uniform distribution of probability. Therefore, the plot b is the only one that shows indication of control by Europa. The observed prominent peaks of probability in the two phase ranges correspond to

the regions in red in plot *a*.

Figure 6.2 - Plots of occurrence probability of the NDA's northern non-Io and non-Ga as a function of Europa's phase angle in different CML ranges.

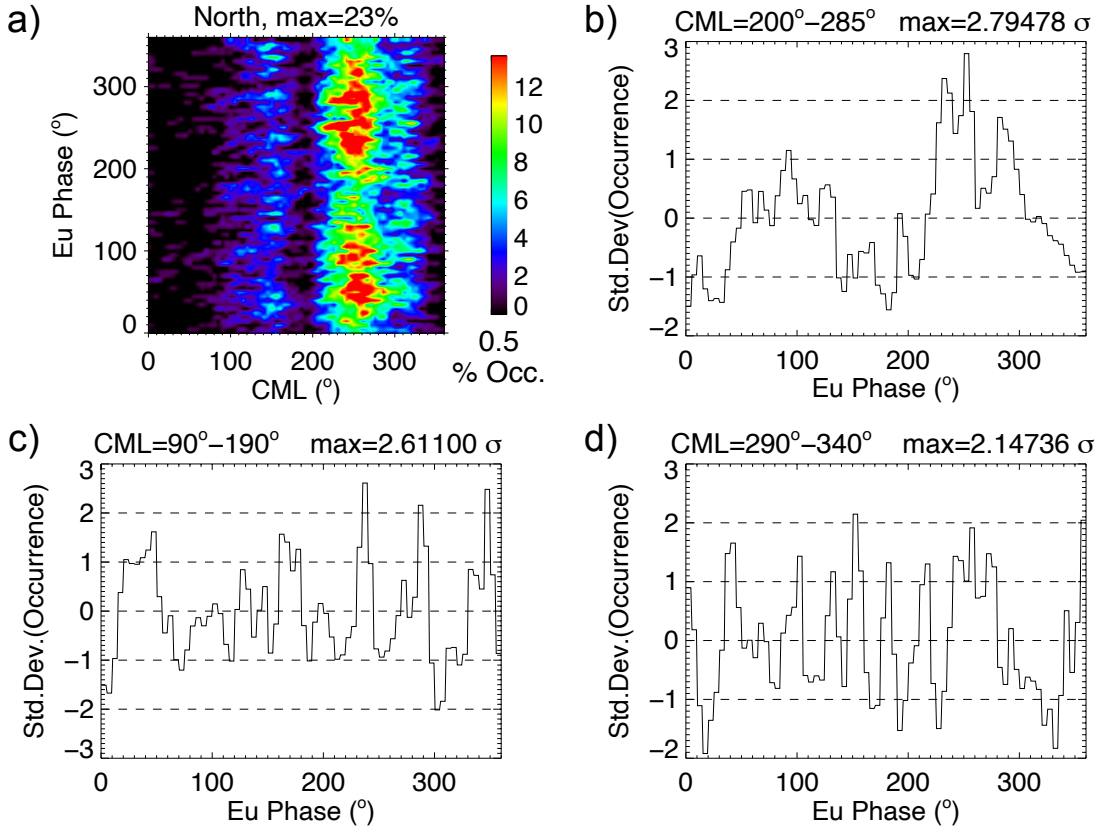

The occurrence probability is given as a function of its standard deviation (σ) in each CML range. σ is distinct for each plot. Each bin corresponds to 5° of Φ_{Eu}.

SOURCE: Author's production.

Similarly, Figure 6.3 shows the plots for the Southern hemisphere. The selected CML intervals were of $290° - 40°$ (*b*), $55° - 195°$ (*c*) and $200° - 285°$ (*d*). Two of these intervals present non-uniform distributions of probability, with prominent peaks: the ones represented in plots *b* and *d*. The prominent peaks in plot *b* occur within the phase intervals of $\sim 20° - 35°$ and $\sim 230° - 270°$, and correspond to the largest red regions in plot *a*. In plot *d*, the prominent peak occur within the phase interval of $\sim 110° - 150°$.

Figure 6.3 - Plots of occurrence probability of the NDA's southern non-Io and non-Ga as a function of Europa's phase angle in different CML ranges.

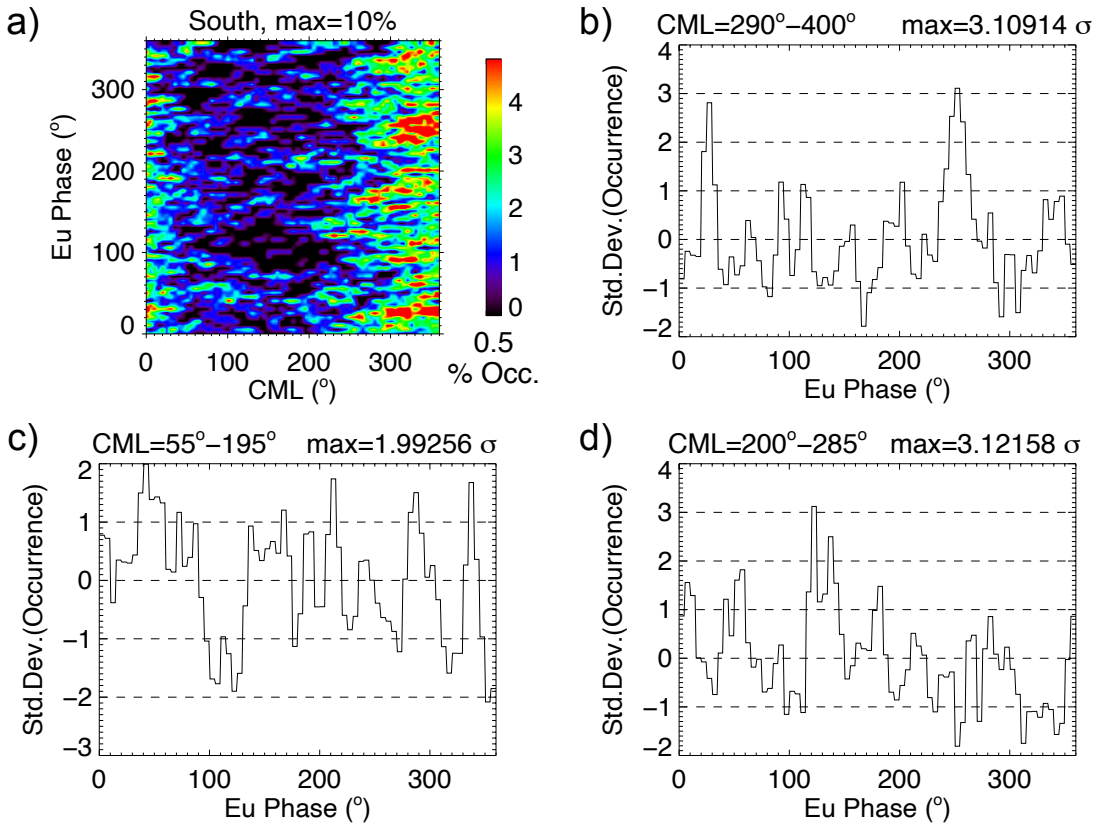

The occurrence probability is given as a function of its standard deviation (σ) in each CML range. σ is distinct for each plot. Each bin corresponds to 5° of Φ_{Eu}.

SOURCE: Author's production

The CML×Φ_{Eu} regions where the prominent peaks of Figure 6.2 and 6.3 are observed were visually selected for analysis of the emissions occurring within them. Figure 6.4 and Figure 6.5 show the peaks highlighted and linked to their corresponding regions in the CML×Φ_{Eu} plane for the jovian Northern and Southern hemispheres, respectively. From the corresponding values of CML and Φ_{Eu}, and the hemisphere of occurrence, some of the peaks were also associated with the probable sources of their emissions on Jupiter's ionosphere, as it is indicated in the figures by the yellow tags. This association was based on the respective CML and satellite's phase ranges of occurrence of Io-DAM, non-Io-DAM and Ga-DAM emissions from each one of the sources on Jupiter presented in previous works (MARQUES et al., 2017; ZARKA et al., 2017; LOUIS et al., 2017; ZARKA et al., 2018).

For the NH (Figure 6.4), two peaks were selected. The peak occurring in $\sim 220° \leq \Phi_{Eu} \leq 260°$, which is the most prominent one in the plot, was associated with the emissions induced by Europa with origin in source A and is referred to as Eu-A now on. The other peak, occurring in $\sim 280° \leq \Phi_{Eu} \leq\sim 300°$, is referred to as *I*. Based on the proximity of the peak *I* to the Eu-A, the peaks may be associated with each other, with their emissions being originated in the same source, A. The phase separation between the peaks might be a consequence of the lack of emissions to complete the "parabolic" pattern. Even so, we will keep referring to the peak *I* as so instead of Eu-A to differentiate them as well as the emissions therein.

Figure 6.4 - Selected peaks of occurrence probability of northern emissions.

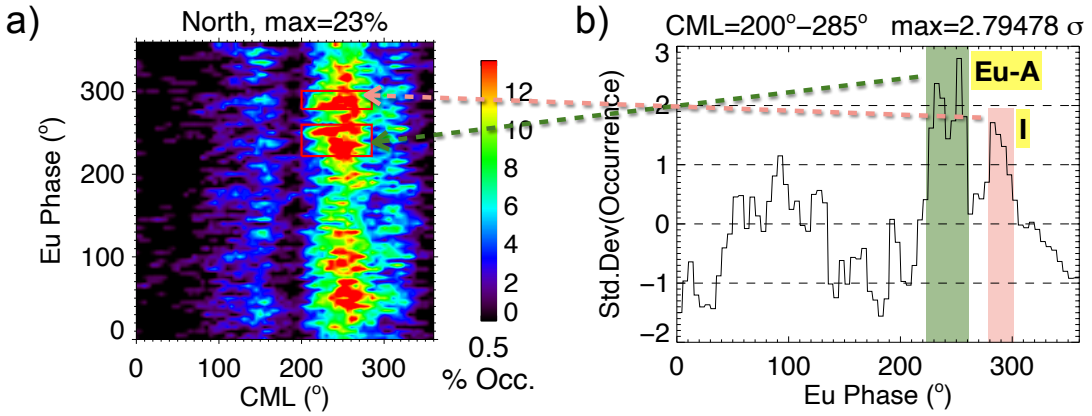

The yellow tags show the new designation for the selected peaks. The emissions of the Eu-A are possible originated in the source A.

SOURCE: Author's production.

For the SH, only the peaks in the interval of $290° \leq \text{CML} \leq 40°$ were considered for further analysis although a prominent peak was also observed in the CML range of $200° \leq \text{CML} \leq 285°$. The peak observed in Figure 6.3 in the plot (d), in $115° \leq \Phi_{Eu} \leq\sim 150°$, has its most prominent part composed by two separated 5° single bins and, therefore, is not statistically significant. For this reason, it was not taken into account for analysis of the emissions therein. Therefore, Figure 6.5 brings the plot only for $290° \leq \text{CML} \leq 40°$, showing the selected peaks and theirs respective regions on the CML$\times\Phi_{Eu}$ plane. Two peaks were selected: one in $\sim 235° \leq \Phi_{Eu} \leq 270°$ and another in $\sim 20° \leq \Phi_{Eu} \leq\sim 35°$. The former case is associated with the emissions induced by Europa from the source C and, therefore, is now on referred to as Eu-C. The last case is not associated with any source and is referred to as *II*.

Figure 6.5 - Selected peaks of occurrence probability of southern emissions.

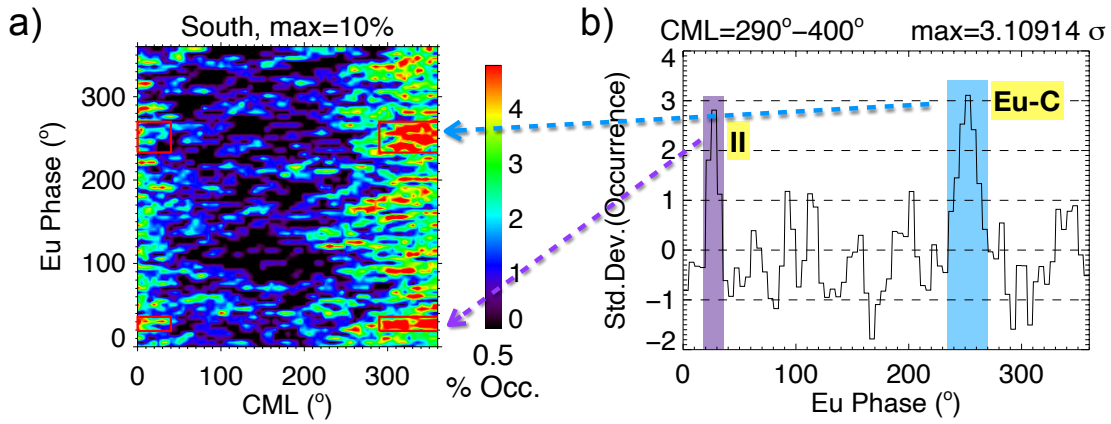

The yellow tags show the new designation for the selected peaks. The emissions of the Eu-C are possible originated in the source C.

SOURCE: Author's production.

7 RESULTS AND DISCUSSION

In this chapter, the maximum frequency, duration and intensity of the selected emissions from the NDA's catalog in our analysis will be presented and discussed. The obtained results will also be compared with results of previous works (as the works of Marques et al. (2017), Louis et al. (2017), Zarka et al. (2018)).

7.1 Analysis of the selected emissions

The emissions occurring within the CML and Φ_{Eu} ranges corresponding to the selected peaks on the data processing work were counted and analyzed. The total number of counted possibly Europa-controlled DAM emissions for the Northern hemisphere (with RH polarization) were 314, while for the Southern hemisphere (with LR polarization), 99 emissions were counted. Those emissions were selected for occurring in the CML and Φ intervals corresponding to the ones of the selected peaks of probability, and, consequently, being possibly induced by the satellite Europa. All the emissions within the peaks were selected on the catalog. The number of emissions in each peak and the corresponding intervals of CML and Φ_{Eu} are presented in Table 7.1.

Table 7.1 - Number of emissions within the selected intervals.

		$\Phi_{Eu}(°)$	CML (°)	N. of Emissions
Northern Hemisphere	Eu-A	222-260	200-285	206
	I	279-301	200-285	108
	TOTAL			314
Southern Hemisphere	Eu-C	233-270	290-400	63
	II	19-36	290-400	36
	TOTAL			99

From the data processing results, the control of part of the jovian DAM by Europa could be more clearly observed on the emissions from the dusk side of Jupiter. No prominent peak of occurrence probability was associated to the B or D sources. The lack of evidence of control of emissions from the dawn side might be due to the smaller amount of samples from this side when compared to the amount of emissions from the dusk side. The plots in Chapter 6 show an accumulation of emissions occurring at the CML range from $\sim 200°$ to $360°$, which corresponds to

the dusk side of Jupiter. Therefore, the sample of emissions from the dusk side for a certain period of time is larger than the sample of the dawn side for the same period, making the detection of control of the emissions from the dawn more difficult. For this reason, the catalog presents evidences of control for the dusk and no significant evidences for the dawn. Consequently, more analyses of the data are needed to enable the observation of the probable control of emissions from Jupiter's dawn side by Europa. The predominance of emissions from the dusk is also observed in the plots for Io and Ganymede (MARQUES et al., 2017; ZARKA et al., 2018), but it did not prevent the observation of Io-DAM and Ga-DAM emissions from the B and D sources probably due to the higher numbers of jovian DAM emissions controlled by each one of these satellites in comparison to the quantity of emissions controlled by Europa.

The distributions of maximum frequency, duration and intensity of the Eu-A and Eu-C are presented in Figure 7.1. The general characteristics of the Europa-dependent emissions were inferred from analysis of the distributions. The analysis was made visually and by the calculation of statistical parameters such as median, mean and standard deviation. From Figure 7.1, we have that the maximum frequency of the Eu-A emissions varies from 16 to 34 MHz, with mode in $\sim$ 25 MHz. For the Eu-C, the maximum frequency varies from 14 to 25 MHz, with mode in $\sim$ 23 MHz. The higher frequencies of the Eu-A emissions over the Eu-C's are due to the higher intensity of the magnetic field in the Northern hemisphere, as already discussed in this work (see Chapter 6). The minimum frequency of the emissions were not analyzed since it is limited by the Earth's ionosphere cut-off frequency.

The duration of the emissions is also observed in Figure 7.1, but it is an aspect of difficult evaluation from the NDA's data because it may be affected by the observation geometry of the emissions and other factors. The emissions are presented on the dynamic spectra as they are detected by the NDA. Since the Array detects the jovian emissions only when the region where it is located on the Earth points to Jupiter, events may be detected after their start and the observation could stop before their end. Therefore, emissions may appear shorter than they really are. That is one of the reasons for the large amount of short duration emissions on the histograms.

The apparent duration of the detected emissions is also affected by the declination of the Earth and by the distance between the Earth and Jupiter. According to Boudjada and Leblanc (1992) and Leblanc et al. (1993), the Earth's declination affects the observed width of the sources along the CML axis on the $\Phi \times$CML plane.

Figure 7.1 - Histograms for maximum frequency, duration and intensity of the possible Eu-A and Eu-C emissions.

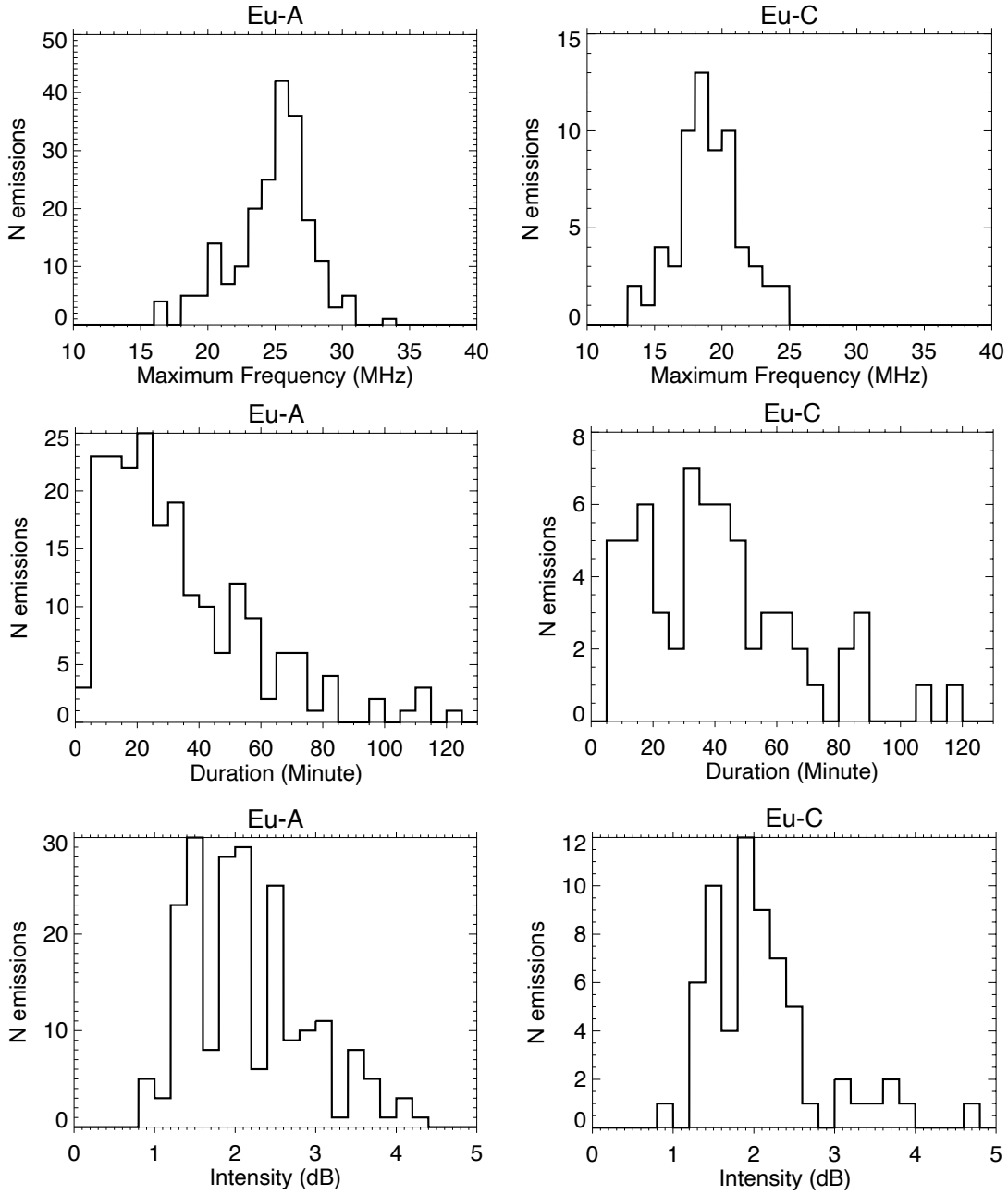

SOURCE: Author's production.

The authors observed that the width of the sources increases as the declination increases, being wider for positive values of declination. In other words, the emissions from each source appear in NDA observations longer in time when the declination

is maximum and shorter when the declination is minimum. Moreover, Zarka et al. (2018) analyzed the jovian DAM emissions on the NDA's catalog, then with 26 years of observations, and showed that the events lasting more than 200 minutes were mainly detected when the Earth-Jupiter distance was less than 5.0 AU. Along the synodic period of the system, this distance varies from 3.95 to 6.45 AU (ZARKA et al., 2018).

Therefore, the duration of the emissions on the catalog depends on several elements, making difficult its analysis. Yet, as the catalog increases along the years, the percentage of short emissions among the entire catalog tends to decrease, improving the evaluation. On the histograms for duration in Figure 7.1, the most common duration varies from 5 to 35 minutes for the Eu-A emissions, and from 5 to 50 minutes for the Eu-C. From these numbers, we may infer that the Eu-C emissions are probably intrinsically longer than the Eu-A.

The other aspect analysed for the selected emissions was the intensity. From Figure 7.1, it can be noted that the values of intensity are similar for both hemispheres, with the most frequent intensities varying from ~ 1.2 dB to ~ 2.6 dB. The difference between the intensities of the Eu-A and the Eu-C is found mainly in their distributions: the intensity of the Eu-A DAM is more widely distributed than the one of the Eu-C. Thus, it is also noticed that the Eu-A emissions have relatively more emissions at high intensity values. The median, mean and standard deviation of the intensity as well as of the maximum frequency and duration of the Eu-A and the Eu-C emissions are presented in Table 7.2.

The parameters in Table 7.2 corresponding to the Eu-A and Eu-C emissions confirm that the Eu-A emissions reach in general higher intensities and maximum frequencies than the Eu-C. The mean, median and standard deviation values for the frequency and the intensity of the Eu-A are higher than the respective values of the Eu-C. The values of standard deviation correspond to the broadness of the distributions, which is larger to the Eu-A emissions probably due to the large amount of samples, possibly also including non-Eu-A emissions. However, with regard to the emissions' duration, the values are higher for the Eu-C, confirming that these emissions must be longer than the Eu-A. The higher standard deviation of the Eu-C, even with less emissions than Eu-A, probably results from the balanced occurrence of long emissions and short emissions, widening the distribution. The significant occurrence of long emissions indicates that the Eu-C emissions must be indeed longer than the Eu-A.

After evaluating the characteristics of the Eu-A and the Eu-C emissions, it is necessary to consider the emissions related to the peaks *I* and *II* in the same aspects, for comparison. Recalling that the emissions *I* are probably from the same source of Eu-A, it was expected that they present similar characteristics to the emissions Eu-A. The statistical parameters for the emissions of peaks *I* and *II* and of the combination of all the selected emissions for each hemisphere are also presented in Table 7.2. The values corresponding to the emissions *I* are close to the respective values of the Eu-A. For this reason, no significant changes are observed in the values of the combination of emissions Eu-A and *I* (in Eu-A + I), in comparison to the values of the Eu-A. The same similarity is also observed between the *II* and the Eu-C emissions, except for the duration, which indicates that the emissions *II* are on average $\sim$ 7 minutes shorter than the Eu-C.

Table 7.2 - Statistical parameters of the possible Eu-A and Eu-C emissions.

	Max.Frequency (MHz)			Duration (min)			Intensity (dB)		
	Med.	Mean	σ	Med.	Mean	σ	Med.	Mean	σ
Eu-A	25.3	24.8	2.90	26.0	33.1	24.1	2.13	2.16	0.736
I	24.9	24.5	2.44	27.0	33.3	24.8	2.19	2.25	0.792
Eu-A + I	25.2	24.7	2.75	27.0	33.2	24.3	2.19	2.19	0.756
Eu-C	18.9	19.0	2.41	37.0	40.8	25.5	1.97	2.12	0.724
II	19.6	19.2	2.77	27.0	33.5	23.5	2.19	2.11	0.649
Eu-C + II	18.9	19.1	2.54	34.0	38.1	24.9	2.00	2.12	0.694

Further, the distributions of maximum frequency, duration and intensity of the emissions *I* and *II* are presented on the histograms in Figure 7.2. This figure also show the distributions related to the Eu-A and the Eu-C emissions as well as the histograms for the complete set of selected emissions separated by their hemisphere of origin: Eu-A plus *I* and Eu-C plus *II*. From a first and preliminary analysis of these histograms, it is observed that the distributions of the emissions *I* behave identically to the ones of the Eu-A, which endorses the idea of direct relation between these two groups of emissions. On the other hand, the distributions of the emissions *II* do not match so well with the Eu-C's, mainly for the duration. This may be associated with the small amount of *II* emissions and/or with the fact that they are originated from a source other than C.

From the similarities between the Eu-A and the *I* emissions and, most importantly, from the proximity between their occurrence along Europa's phase, we suggest that they constitute together a possible Eu-A emissions. However, because of the gap between the peaks, the emissions *I* may be related to a A' source, following Marques et al. (2017), who observed new regions of control by Io and labeled them adding one or more apostrophes to the source letter to differentiate them from the usual A, B, C and D sources. However, more analyses are needed to test this hypothesis.

7.2 Occurrence probability of the emissions by maximum frequency intervals

After the analysis of the distributions of all the selected emissions in this work, we selected the most common frequencies in the histograms of Figure 7.2 for a new analysis of occurrence probability of the emissions taking into consideration their maximum frequency (f_{max}). This analysis considers only the maximum frequency because it is the only parameter that is not affected by the observation geometry and brings information about the magnetic field at the source location on Jupiter.

For the emissions coming from the North hemisphere, the most common values of maximum frequency are in the range of 24 - 27 MHz. Then, the new plots of occurrence probability considered only the emissions with 24 MHz $\leq f_{max} <$ 27 MHz. These plots are presented in Figure 7.3. From the plot *b*, we may infer that most of the emissions induced by Europa related to peaks Eu-A and *I* have indeed frequencies in this range since the peaks are still very prominent. Other peaks, not as prominent as the Eu-A and *I*, also appear within the Φ_{Eu} interval of $50° - 120°$, suggesting that Europa might control emissions with similar maximum frequency also in these phase angles of its orbit.

Besides that, the new plots of Figure 7.3 present a peak that was not seen before in the CML range of $90° - 190°$ (plot *c*). This peak occurs within the Φ_{Eu} interval of $20° - 40°$ and is now on referred to as peak *III*. The absence of peak *III* in the previous plots and its presence now suggest that the possible control by Europa in this region is specifically over emissions with maximum frequency between 24 MHz and 27 MHz.

After that, other plots of occurrence probability were set considering all the emissions with maximum frequency out of the interval of 24 - 27 MHz in order to observe the control of these emissions by Europa. On these new plots, which are presented in Figure 7.4, only emissions with $f_{max} <$ 24 MHz or $f_{max} \geq$ 27 MHz were considered.

Figure 7.2 - Histograms of characteristics of the emissions Eu-A, Eu-C, I, II, and of the entire set of selected emissions from each hemisphere.

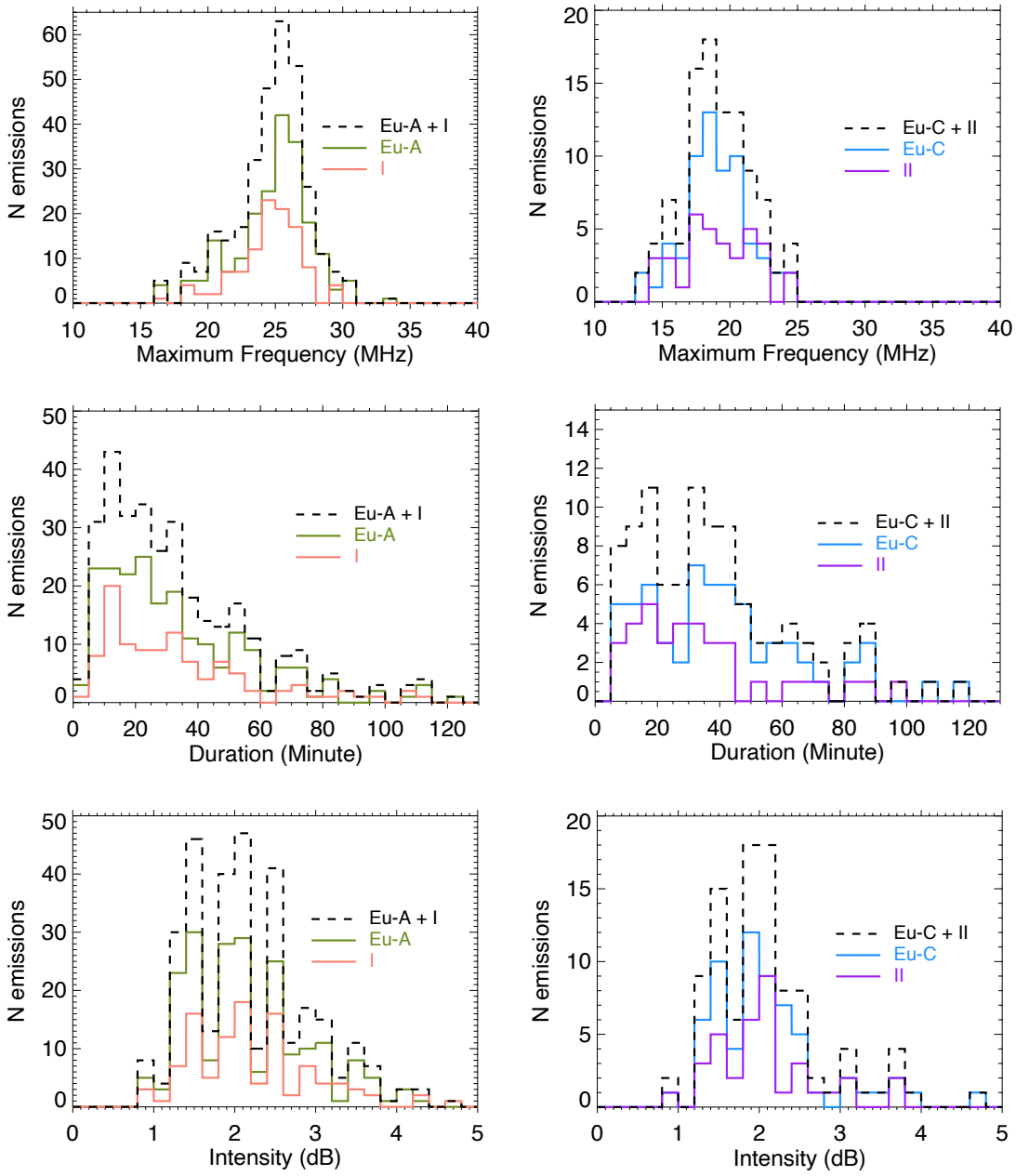

SOURCE: Author's production.

On the plot b, we see a roughly harmonic behaviour of the probabilities along the phase of Europa, with peaks of similar amplitude, disregarding the one bin reaching $\sim 3\sigma$. This behaviour has been observed in all the plots of the North hemisphere

for the CML range of $200° - 285°$. However, all the previous related plots had peaks that were prominent even over this harmonic behaviour (the Eu-A and the I), which are not well observed here (see again Figure 6.2). From this result, it is suggested that the emissions induced by Europa in the peaks Eu-A or I are only some of the emissions with maximum frequency from 24 to 27 MHz, which correspond to a total of 164 emissions. Part of the other emissions, whose occurrence appears harmonically, might result from other periodic factors. These factors may include satellite's orbit, Jupiter's and/or Earth's day and year, and the jovian rotation, among other possibilities.

Figure 7.3 - Occurrence probability of all the Northern emissions with $24 \leq f_{max} < 27$ (MHz).

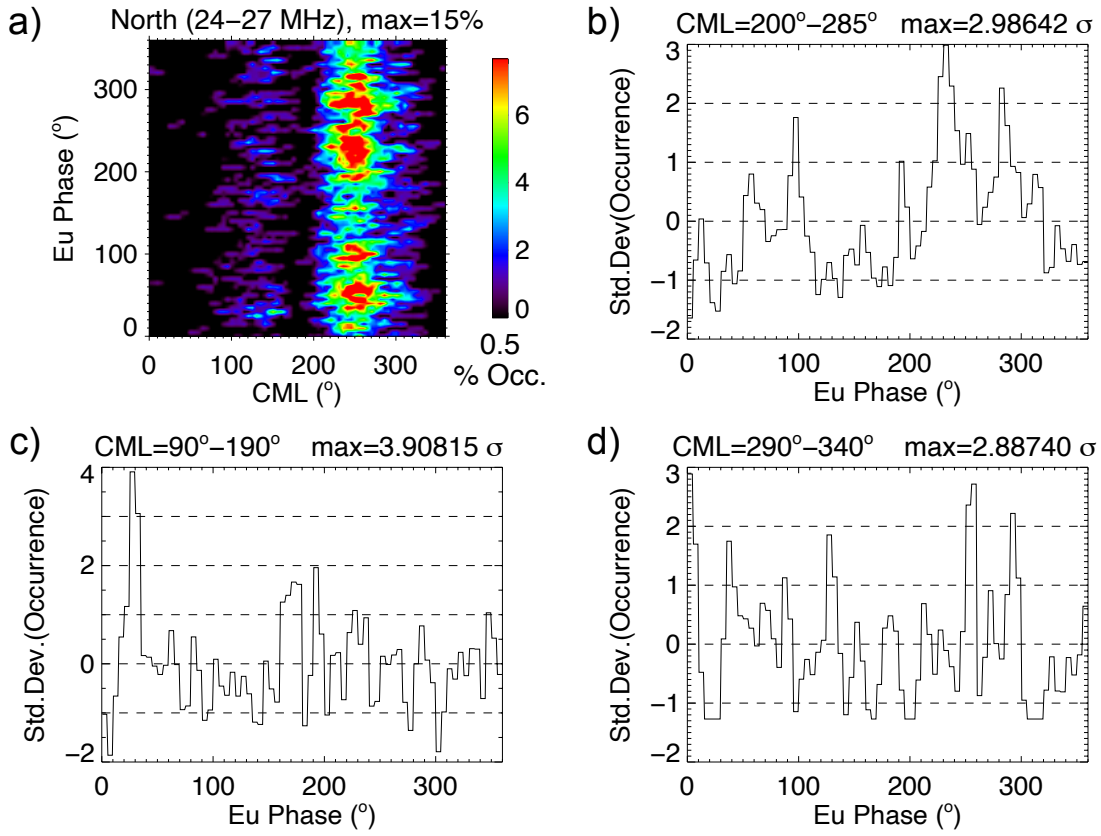

SOURCE: Author's production.

Similarly, the analysis of the occurrence probabilities considering different intervals of maximum frequency was applied to the emissions originated in the South hemisphere. The most common frequencies in the histograms of Figure 7.2 for the

Eu-C were in the range of 17 - 21 MHz. Therefore, only the emissions with 17 MHz $\leq f_{max} <$ 21 MHz were considered and are shown in the plots in Figure 7.5. From these plots, it is possible to observe that the control of these frequencies by Europa occurs only in the region of the peak Eu-C, suggesting that the emissions of the peak *II* that are induced by Europa have maximum frequencies out of this range.

Figure 7.4 - Occurrence probability of the Northern emissions with $f_{max} <$ 24 MHz or $f_{max} \geq$ 27 MHz.

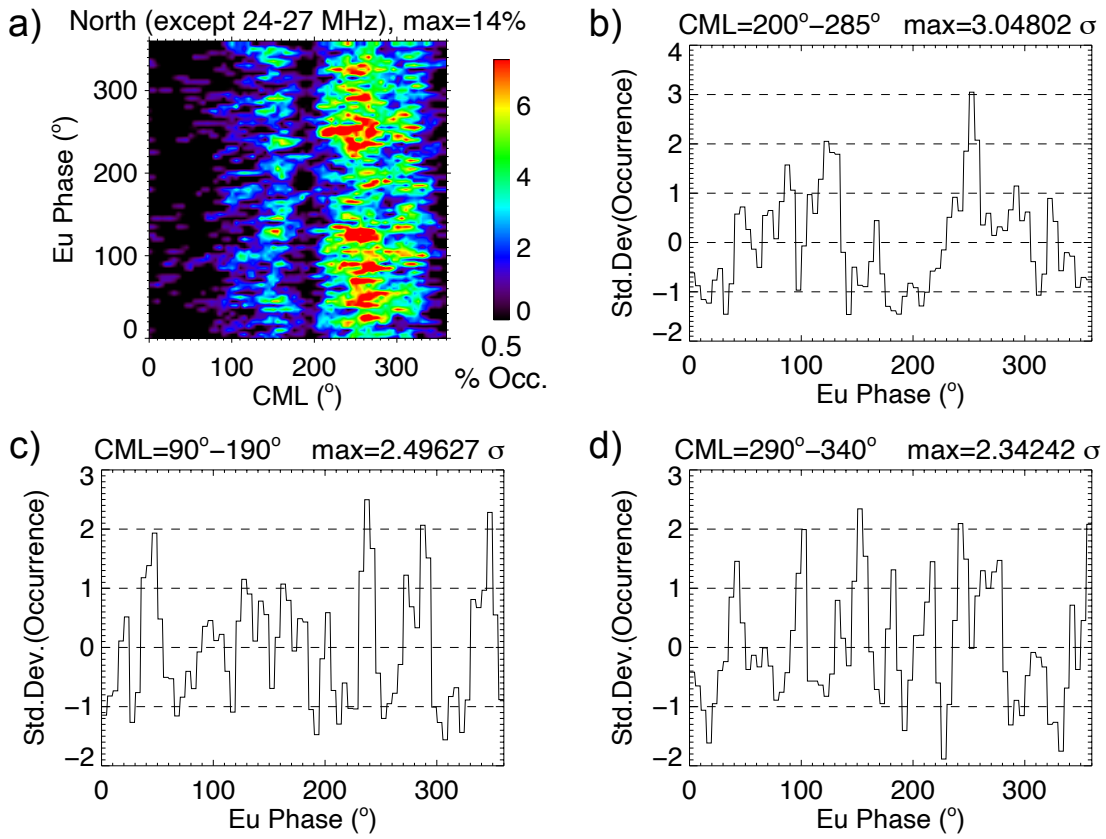

SOURCE: Author's production.

In order to check the maximum frequency of the emissions induced by Europa within the peak *II*, the plots were redone for emissions with maximum frequency in a different range. From the distribution of frequencies of the emissions *II* in Figure 7.2, the new selected range of frequency was from 21 to 23 MHz, which is the most common range in the distribution after the previous selected range. Therefore, the new plots, presented in Figure 7.6, were set with emissions with 21 MHz $\leq f_{max} <$ 23 MHz. From the plots *a* and *b*, it is observed that the control of the emissions

by Europa occurs in the phases associated not only with the peak *II* but also for Eu-C. For this reason, it is suggested that the emissions within the peak Eu-C that are induced by Europa have maximum frequencies from 17 to 23 MHz, while the ones occurring within peak *II* have maximum frequencies from 21 to 23 MHz. The number of emissions with maximum frequency in the range of 17-23 MHz within the peak Eu-C is 49.

Figure 7.5 - Occurrence probability of the Southern emissions with $17 \leq f_{max} < 21$ (MHz).

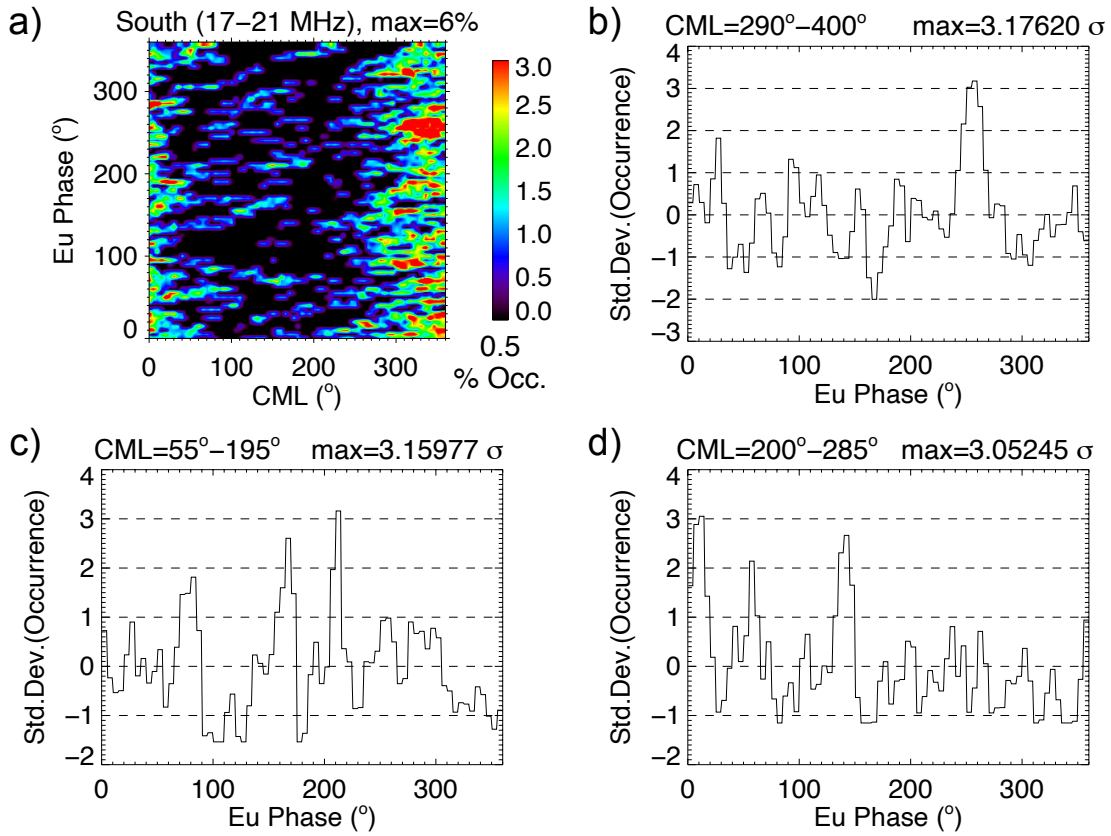

SOURCE: Author's production.

After this analysis, it is suggested that the emissions of peak *II* might be related to a C' source, following what was previously discussed regarding the emissions of the peak *I* being possibly originated in a A' source. However, due mainly to the significant phase distance between their respective peaks in the plots, the emissions *II* will not be combined with the Eu-C in this work, contrarily to what occurred to the Eu-A and the *I*. The hypothesis of origin in a C' source needs to be tested

through more analysis.

Figure 7.6 - Occurrence probability of the Southern emissions with $21 \leq f_{max} < 23$ (MHz).

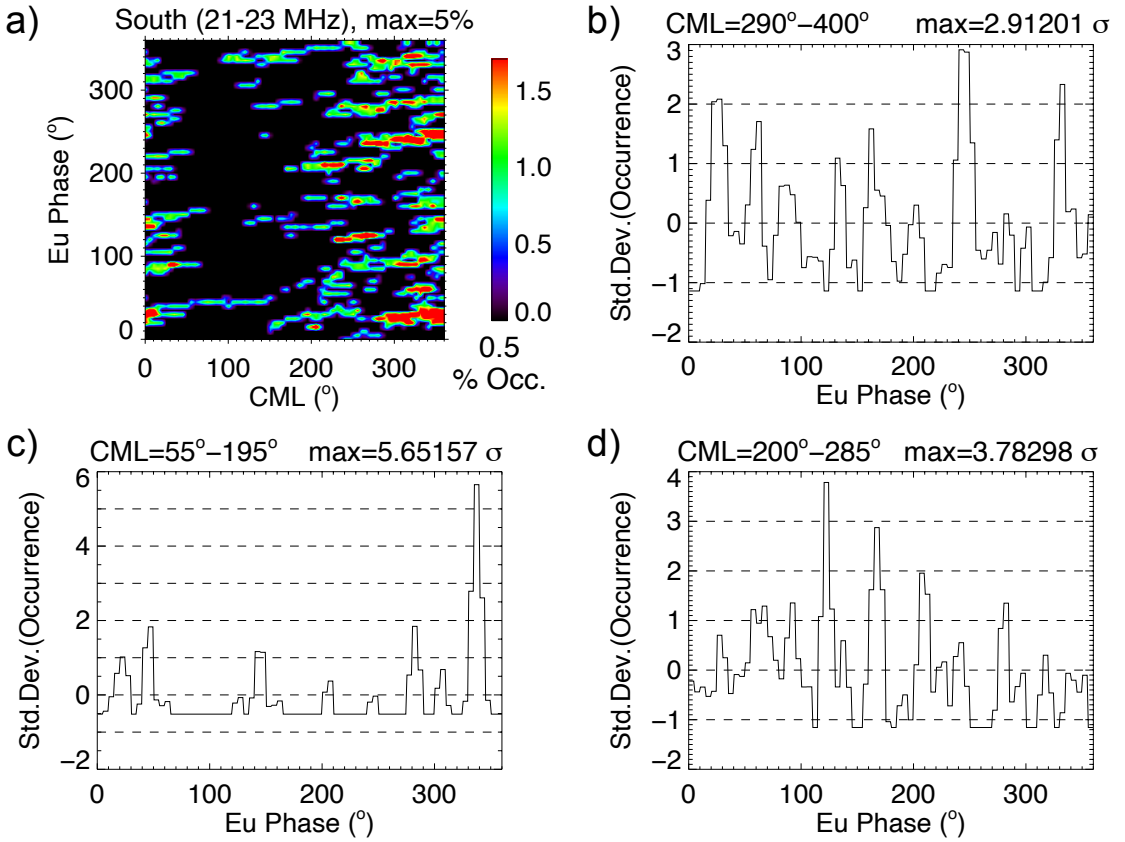

SOURCE: Author's production.

The statistical parameters of the distributions of maximum frequency, duration and intensity of the emissions selected from the analysis of the emissions' maximum frequency (164 emissions within Eu-A or I and 49 emissions within peak Eu-C) are shown in Table 7.3. The values for the same parameters that were calculated for all the emissions occurring within the selected peaks, regardless of their maximum frequency, are also shown for comparison. The emissions of peaks Eu-A and I appear already together because of their similarity and proximity. Besides the already expected changes in the values for maximum frequency after the analysis of frequency, the general duration of the emissions increased significantly, mainly for the Eu-C emissions, indicating a mean difference of almost 10 minutes between the emissions induced by Europa with origin in the A source and the ones originated in the C

source.

Table 7.3 - Statistical parameters of the Eu-A and Eu-C emissions before and after the analysis of maximum frequency.

	Max.Frequency (MHz)			Duration (min)			Intensity (dB)		
	Med.	Mean	σ	Med.	Mean	σ	Med.	Mean	σ
Eu-A + I	25.2	24.7	2.75	27.0	33.2	24.3	2.19	2.19	0.756
Eu-C	18.9	19.0	2.41	37.0	40.8	25.5	1.97	2.12	0.724
After Max. Frequency Analysis									
Eu-A + I	25.5	25.5	0.816	28.0	35.0	26.2	2.19	2.25	0.789
Eu-C	19.1	19.3	1.48	41.0	44.6	24.8	1.96	2.05	0.660

7.3 Comparison with Eu-A and Eu-C emissions on other databases and with Io-DAM and Ga-DAM on the NDA's catalog

Finally, our results were compared with the Europa-dependent emissions originated in the sources A and C that were selected by Louis et al. (2017) from the database of Voyager 1 and 2 and Cassini. Table 7.4 brings the amount of Eu-A and Eu-C emissions detected in each database, with the minimum and maximum values, median and standard deviation of the maximum frequency and duration of the emissions. With regard to the NDA's catalog, the Eu-A emissions correspond to the emissions of the peaks Eu-A and *I* in this work, while the Eu-C corresponds to the emissions within the peak Eu-C only. The upper part of the values of NDA's catalog refers to all the emissions occurring within the peaks regardless of the analysis of maximum frequency, while the bottom part shows the values for the emissions selected from the peaks after this analysis.

From Table 7.4, it is observed that the selection of the emissions on the NDA's catalog regarding their maximum frequency approached the medians of duration to the ones observed by Louis et al. (2017) on Cassini's data, more strongly for the Eu-C emissions. It is also observed that the general medians of maximum frequency on the NDA's catalog are higher than the medians on the other catalogs (mainly Cassini), even without considering the analysis of frequency, which slightly increased the medians. This is caused by the fact that the frequency receivers on Cassini were sensible to frequencies up to 16.125 MHz only, while the receivers of the Voyagers

and the NDA could detect the highest frequencies of the jovian DAM (LOUIS et al., 2017). Further, the frequencies detected by the NDA are bounded by the cut-off frequency of the Earth's ionosphere, which may contribute to the higher medians of the NDA. Over Nançay, the lowest ionosphere cut-off frequency is of $\sim$ 10 MHz (BOISCHOT et al., 1980), limiting the observation to emissions with $f_{max} > 10$ MHz.

Table 7.4 - Comparison to data from Voyager and Cassini spacecraft.

			Max. Frequency (MHz)	Duration (min)
			Median$\pm\sigma$	Median$\pm\sigma$
		Number	[Min-Max]	[Min-Max]
Voyager	Eu-A	6	22.0 ± 8.5	35.0 ± 18.1
			[12.0-34.0]	[15.0-60.0]
	Eu-C	2	-	-
			[13.0-13.5]	[55.0-100.0]
Cassini	Eu-A	23	16.0 $\pm$2.4	40.0 $\pm$12.3
			[6.0-16.0]	[20.0-80.0]
	Eu-C	29	13.0 ± 2.8	40.0 ± 23.3
			[7.25-16.0]	[20.0-105.0]
NDA's catalog	Eu-A	314	25.2 ± 2.7	27.0 ± 24.3
			[16.3-33.1]	[2.0-123.0]
	Eu-C	63	18.9 ± 2.4	37.0 ± 25.5
			[13.7-24.8]	[6.0-118.0]
	After Max. Frequency Analysis			
	Eu-A	164	25.5 ± 0.82	28.0 ± 26.2
			[24.1-26.9]	[2.00-123]
	Eu-C	49	19.1 ± 1.5	41.0 ± 24.8
			[17.1-22.3]	[7.0-118.0]

Source: Louis et al. (2017).

After all the analyses on different aspects of the possible Eu-DAM on the NDA's catalog, the comparison of the emissions selected in this work with all the emissions already selected and classified on the catalog (either induced by Ganymede or Io) is an interesting possibility enabled by the digital format of the Array's data. For

this comparison, the distributions of maximum frequency, duration and intensity of the Io-A and -C, Ga-A and -C and Eu-A and -C emissions were plotted together, as shown in Figure 7.7. On these plots, the emissions Eu-A correspond to all the emissions occurring within the peaks Eu-A and *I*; and the emissions Eu-C, to all the emissions occurring within the peak Eu-C.

From a first analysis of the histograms for the emissions from the A source, it is easily noticed that there are more Eu-A than Ga-A emissions even though the control by Ganymede was more easily detected, having been identified earlier. In contrast, on the histograms for the C source, the Europa-induced emissions correspond to the smallest amount on the plot. The relative small amount of Ga-A emissions is due to the fact that no strong evidence of the control by Ganymede could be observed in the most active CML range, from 200° to 280°. Therefore, the Ga-A emissions are only the ones that indicate control by Ganymede out of this range (ZARKA et al., 2017; ZARKA et al., 2018). On the other hand, the Io-induced emissions are predominant among the emissions in both cases of the A source and of the C source.

In a more quantitative analysis of the distributions, the maximum frequencies of the emissions from the source A probably induced by Europa and Ganymede have similar mean maximum frequency, with the majority of the Europa-A emissions reaching values only slightly higher than the most common frequencies of the Ganymede-A emissions. The similarity between these values may be due to the proximity of Europa's and Ganymede's northern footprints on Jupiter's atmosphere, as shown in Figure 2.3. According to Zarka et al. (2018), the northern Ga-DAM emissions have lower maximum frequency than the northern Io-DAM because Io's flux tube footprint is southward from Ganymede's, crossing the northern anomaly of high-amplitude magnetic field on the jovian surface. Taking into account this fact, we may infer that the frequencies of the Eu-A are roughly higher than the Ga-A because Europa is closer to Jupiter in comparison to Ganymede. Therefore, the footprint of Europa's flux tube must lay between Io's and Ganymede's footprints, in a region closer to the anomaly than Ganymede's and, consequently, with magnetic field intensity slightly higher than the intensity at Ganymede's footprint. Besides that, other factor that affects the maximum frequency of the emissions is the point of emissions beaming along the magnetic field lines, which is lower for the Io-DAM (MARQUES et al., 2017). This may explain why the maximum frequency of the Io-DAM is still larger than the Eu-C in the southern hemisphere.

Figure 7.7 - Distribution of maximum frequency, duration and intensity of the emissions induced by Io, Ganymede and Europa (from sources A and C) present on the NDA's catalog.

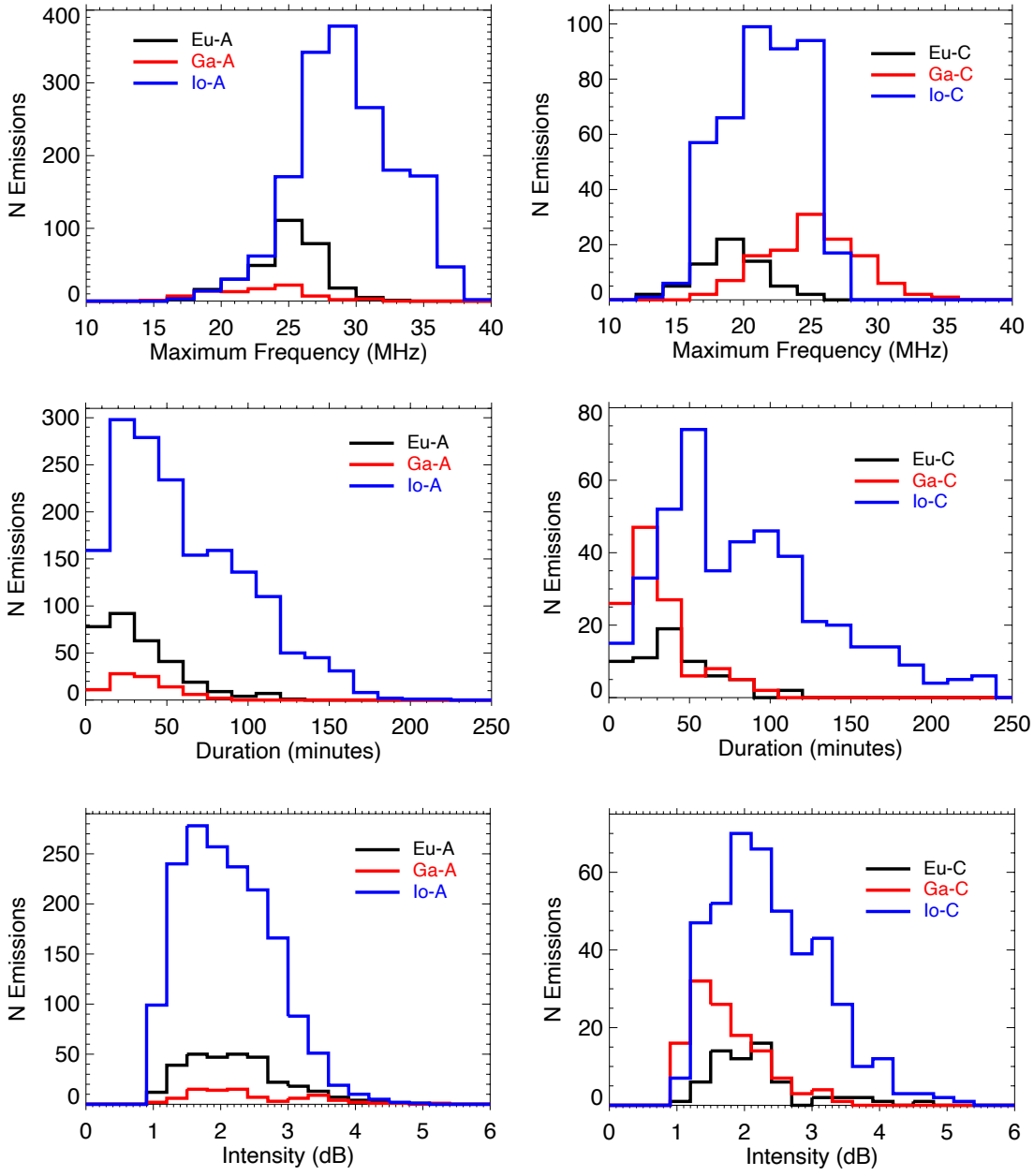

SOURCE: Author's production.

For the Southern hemisphere, the Ga-C emissions shows the highest values of maximum frequency, which may be caused by the absence of an anomaly of high-amplitude magnetic field on the southern hemisphere. In this case, the intensity

of the magnetic field must increase with the magnetic latitude, reaching its maximum values close to the magnetic pole. Since Ganymede is the farthest satellite to Jupiter in comparison to Io and Europa, its flux tube's southern footprint must lay on Jupiter's atmosphere in the highest latitude, in a region of more intense magnetic field. This hypothesis needs to be tested taking into account the topology of the jovian magnetic field.

The distributions of the emissions' duration show a predominance of the short emissions for both Io-, Ga- and Eu-dependent emissions, regardless of their hemisphere of occurrence. As discussed earlier in this work, this predominance may not represent the reality of the emissions' duration. However, we note on these distributions that the Io-DAM emissions are overall longer in time than the Eu-DAM and Ga-DAM. Between the Eu-DAM and Ga-DAM, the Eu-A emissions seem to be longer than the Ga-A, which may be due to the nature of factors affecting the electrodynamic interactions and controlling the emissions' occurrence.

Ganymede has an intrinsic magnetic field, which configures a magnetosphere similar to the Earth's inside of Jupiter's magnetosphere. In this context, the interaction with the jovian magnetospheric plasma is affected by magnetic reconnection, which opens Ganymede's magnetic field lines, enabling plasma entrance in the magnetosphere and, consequently, changing the plasma density in the vicinity of Ganymede (GRASSET et al., 2013). On the other hand, the electromagnetic interaction between Europa and Jupiter is affected by the Alfvénic interaction (KIVELSON et al., 2004). Therefore, taking into account the different interactions, it may be suggested that the emissions' duration is a reflection of the endurance time of the variations in the system that contributed to their origin. However, this is only a hypothesis.

Finally, with regard to the intensity of the emissions, the histograms of Figure 7.7 show that the northern emissions have on average higher values than the southern emissions, except for the Io-DAM, which present similar distributions in both hemispheres. The Io-DAM from the southern hemisphere are overall more intense than the southern Ga-DAM and Eu-DAM emissions. However, no significant difference is observed in the intensities in the northern hemisphere. Furthermore, the most common values of intensity of the Ga-C are smaller than the ones for the Eu-C, suggesting that the southern emissions induced by Ganymede are less intense than the ones induced by Europa.

8 CONCLUSIONS AND FUTURE WORKS

In this Master's dissertation, the extensive catalog of the Nançay decameter array was analyzed in order to detect the control of the jovian Decametric (DAM) radio emissions by the satellite Europa, as an extension of the analysis of Zarka et al. (2017). By disregarding the emissions induced by the satellites Io and Ganymede in the analysis, it was possible to observe evidences of control of both emissions from the North and the South hemispheres of Jupiter by Europa. The evidences were, however, more clearly observed regarding the control of emissions from the sources of the dusk side, A and C. More analyses are still needed to better observe and confirm the control by Europa on the emissions from the jovian dawn side on the NDA's catalog.

In total, 413 emissions were selected as being possibly controlled by Europa, from which 314 were from the North hemisphere and 99 from the South. The northern emissions occurred on the $\Phi_{Eu}\times$ CML plane in two different Φ_{Eu} regions, referred to as Eu-A and *I* in this work. These regions are both located in the same interval of CML, from 200° to 285°, and are separated from each other by a small gap of $\sim 20°$ along Φ_{Eu}' axis. Similarly, the selected southern emissions occurred in two different Φ_{Eu} regions on the plots, which were referred to as Eu-C and *II*. Both regions are located in the CML range from 290° to 40°, but separated along the phase's axis by a gap of $\sim 200°$.

The CML and Europa's phase ranges referred to as Eu-A and Eu-C were nominated after the respective probable source of their emissions, A and C, respectively. The classification of the source was based on the intervals of CML where the jovian DAM emission from each source is detected when observed from the Earth's surface, taking previous works as references. Both the A and C sources are located in the dusk side of Jupiter.

From the distributions of maximum frequency of the emissions, it was observed that the majority of the Eu-A has maximum frequencies in the range of 24-27 MHz, with average of 24.8 MHz and median of 25.3 MHz, while the majority of the Eu-C emissions has maximum frequencies in the range of 17-21 MHz, with average of 19 MHz and median of 18.9 MHz. The distributions of duration and intensity of the emissions were also analyzed and indicated that the Eu-C emissions are longer in time and slightly less intense than the Eu-A emissions. The Eu-C emissions have average duration of 40.8 min and median of 37.0 min, while the Eu-A emissions have average duration of 33.1 min and median of 26.0 min. For the intensity, the average

and median of the Eu-C are, respectively, 2.12 dB and 1.97 dB, and for the Eu-A, 2.26 dB and 2.13 dB.

The distributions for the same aspects considered in the analysis of the Eu-A and the Eu-C emissions were also analyzed for the emissions in the regions *I* and *II*. The histograms and statistical parameters of the *I* emissions showed a strong similarity to the ones of the Eu-A emissions, indicating that those emissions may have a coincident source with the Eu-A emissions or be originated on an A' source, in similar conditions to the A source. The histograms and statistical parameters of the emissions *II*, although still similar to the Eu-C emissions, did not show the same similarity observed between the Eu-A and *I*, mainly in the duration of the emissions. The Eu-C emissions are on average 7 minutes longer than the emissions of the type *II*.

From analyses of occurrence probability of the emissions on the NDA's catalog by taking into account the emissions' maximum frequency, it was observed that the satellite Europa induces the emissions with maximum frequency in the range of 24-27 MHz for the emission types Eu-A and *I*, corresponding to a total of 164 events, and emissions with maximum frequency in the range of 17-23 MHz for the type Eu-C, which correspond to 49 events. For the emissions *II*, the control of Europa was observed only over emissions with maximum frequency between 21 and 23 MHz. However, this analysis is statistical and needs more studies to confirm it.

The emissions *II* were pointed as being possibly associated with a source C', but, differently to the emissions *I*, which were presented later on combined to the Eu-A, they were not combined to the Eu-C emissions in this work. This was due mainly to the significant gap in the satellite's phase between their regions of occurrence on the plots.

By comparison between the Eu-DAM emissions observed on the NDA's catalog and the emissions detected by Louis et al. (2017) on the databases of the Voyager 1 and 2, and Cassini, the Eu-A and the Eu-C emissions on the NDA's catalog seem to have higher frequency and to be shorter in time than the same type emissions on the other databases, which probably result from the limitations imposed by the geometry of the observation from the Earth and by limitations of Cassini's frequency receivers. Yet, the same relation between the Eu-A and Eu-C emissions with regard to their duration and frequency was observed on all the catalogs: The Eu-A emissions are shorter in time and have higher maximum frequencies than the Eu-C emissions.

Moreover, by comparison with the Io-DAM and the Ga-DAM emissions on the NDA's catalog, it was observed that the Eu-A emissions reach maximum frequencies slightly higher than the ones reached by the Ga-A emissions, and that both have maximum frequencies lower than the Io-A's. For the southern hemisphere, the Ga-C emissions are the ones with higher values of maximum frequency, followed by the Io-C and finally the Eu-C emissions. With regard to the duration, the Io-C emissions are the longest emissions. Between the distributions for duration of the Eu-DAM and the Ga-DAM, no significant difference was observed, but still both the Eu-A and the Eu-C seem to be longer than the Ga-A and the Ga-C emissions, which may be a reflection of the different types of plasma interaction occurring near Ganymede and Europa. Besides that, regarding the emissions' intensity, the Eu-C is shown to be more intense than the Ga-C type. For the northern hemisphere, however, all the emission group types present similar distributions of intensity.

From the results obtained in this work, it was possible to identify with great statistical significance the control by Europa of part of Jupiter's DAM emissions. Further, jovian DAM emissions from the dusk North and South hemispheres, Eu-A and Eu-C, were identified and well characterized. Statistical distribution parameters for their maximum frequency, duration and intensity have been found for the first time.

For future research, it is intended to perform the refinement of the results through the study of the arc patterns of the emissions Eu-A, Eu-C, *I* and *II* on the dynamic spectra. Through this analysis, it is expected that we will be able to improve the selection of the emissions induced by Europa among all the possible emissions statistically selected and to confirm the probable source of the emissions *I* and *II*.

Other subject to be done is the search of the signature of Europa's orbital period, of about 3.5 days, in the NDA's catalog. This research should be conducted applying Lomb-Scargle techniques.

Further research points worth to pursue in future work is to compare NDA's observations of Eu-DAM with JUNO mission radio observations, and to compare both NDA's and JUNO's data with jovian models of radio arcs, as the ones simulated by the ExPRES.

REFERENCES

ANDERSON, J. D.; SCHUBERT, G.; JACOBSON, R. A.; LAU, E. L.; MOORE, W. B.; SJOGREN, W. L. Europa's differentiated internal structure: inferences from four Galileo encounters. **Science**, v. 281, n. 5385, p. 2019–2022, 1998. 17

AUBIER, M.; BOISCHOT, A.; DAIGNE, G.; LEBLANC, Y.; LECACHEUX, A.; DE LA NOË, J.; MØLLER-PEDERSEN, B.; ROSOLEN, C. Project of a large collecting array at Nançay. In: MEETINGS OF CESRA, 5., 1975, Mulhouse, France. **Proceedings**. Florence: European Physical Society, 1975. p. 110. 36, 37

BAGENAL, F. The magnetosphere of Jupiter: coupling the equator to the poles. **Journal of Atmospheric and Solar-Terrestrial Physics**, v. 69, n. 3, p. 387–402, 2007. 1, 6, 15

BAGENAL, F. et al. Magnetospheric science objectives of the Juno mission. **Space Science Reviews**, v. 213, n. 1-4, p. 219–287, 2017. 6, 7, 33

BAGENAL, F.; SULLIVAN, J. D. Direct plasma measurements in the Io torus and inner magnetosphere of Jupiter. **Journal of Geophysical Research: Space Physics**, v. 86, n. A10, p. 8447–8466, 1981. 2

BHATTACHARYYA, D.; CLARKE, J. T.; MONTGOMERY, J.; BONFOND, B.; GÉRARD, J.-C.; GRODENT, D. Evidence for auroral emissions from Callisto's footprint in HST UV images. **Journal of Geophysical Research: Space Physics**, v. 123, n. 1, p. 364–373, 2018. 7

BIGG, E. K. Influence of the satellite Io on Jupiter's decametric emission. **Nature**, v. 203, n. 4949, p. 1008–1010, 1964. 1, 8, 9

BOISCHOT, A.; ROSOLEN, C.; AUBIER, M. G.; DAIGNE, G.; GENOVA, F.; LEBLANC, Y.; LECACHEUX, A.; DE LA NOË, J.; MØLLER-PEDERSEN, B. A new high-grain, broadband, steerable array to study jovian decametric emission. **Icarus**, v. 43, n. 3, p. 399–407, 1980. 22, 35, 36, 59

BOUDJADA, M. Y.; LEBLANC, Y. The variability of jovian decametric radiation from 1978 to 1988. **Advances in Space Research**, v. 12, n. 8, p. 95–98, 1992. 48

BURKE, B. F.; FRANKLIN, K. L. Observations of a variable radio source associated with the planet Jupiter. **Journal of Geophysical Research**, v. 60, n. 2, p. 213–217, 1955. 1, 5

CARR, T. D.; DESCH, M. D.; ALEXANDER, J. K. Phenomenology of magnetospheric radio emissions. In: DESSLER, A. J. (Ed.). **Physics of the jovian magnetosphere**. Cambridge: Cambridge University Press, 1983. v. 1, p. 226–284. 6

CLARKE, J. T. Auroral processes on Jupiter and Saturn. In: KEILING, A.; DONOVAN, E.; BAGENAL, F.; KARLSSON, T. (Ed.). **Auroral phenomenology and magnetospheric processes: Earth and other planets**. Washington, DC: AGU, 2012. p. 113. 7, 8

CLARKE, J. T.; AJELLO, J.; BALLESTER, G.; JAFFEL, L. B.; CONNERNEY, J.; GéRARD, J. C.; GLADSTONE, G. R.; GRODENT, D.; PRYOR, W.; TRAUGER, J.; WAITER JR, J. H. Ultraviolet emissions from the magnetic footprints of Io, Ganymede and Europa on Jupiter. **Nature**, v. 415, n. 6875, p. 997–1000, 2002. 7, 8, 21

CLARKE, J. T.; BALLESTER, G.; TRAUGER, J.; AJELLO, J.; PRYOR, W.; TOBISKA, K.; CONNERNEY, J. E. P.; GLADSTONE, G. R.; WAITE JR, J. H.; JAFFEL, L. B.; GÉRARD, J.-C. Hubble Space Telescope imaging of Jupiter's UV aurora during the Galileo orbiter mission. **Journal of Geophysical Research: Planets**, v. 103, n. E9, p. 20217–20236, 1998. 21

CLARKE, J. T.; GRODENT, D.; COWLEY, S. W. H.; BUNCE, E. J.; ZARKA, P.; CONNERNEY, J. E. P.; SATOH, T. Jupiter's aurora. In: MCKINNON, W. B.; DOWLING, T. E.; BAGENAL, F. (Ed.). **Jupiter: the planet, satellites and magnetosphere**. New York: Cambridge University Press, 2004. v. 1, p. 639–670. 1, 5, 6, 7, 14, 25

CONNERNEY, J. E. P.; KOTSIAROS, S.; OLIVERSEN, R. J.; ESPLEY, J. R.; JØRGENSEN, J. L.; JOERGENSEN, P. S.; MERAYO, J. M. G.; HERCEG, M.; BLOXHAM, J.; MOORE, K. M.; BOLTON, S. J.; LEVIN, S. M. A new model of Jupiter's magnetic field from Juno's first nine orbits. **Geophysical Research Letters**, v. 45, n. 6, p. 2590–2596, 2018. 41

CRARY, F. J. On the generation of an electron beam by Io. **Journal of Geophysical Research: Space Physics**, v. 102, n. A1, p. 37–49, 1997. 14

CRARY, F. J.; BAGENAL, F. Coupling the plasma interaction at Io to Jupiter. **Geophysical Research Letters**, v. 24, n. 17, p. 2135–2138, 1997. 1, 2, 13, 15

DULK, G. A. Lack of effects of satellites Europa, Ganymede, Callisto, and Amalthea on the decametric radio emission of Jupiter. **The Astrophysical Journal**, v. 148, p. 239, 1967. 2, 20

_____. Radio emission from the Sun and stars. **Annual Review of Astronomy and Astrophysics**, v. 23, p. 169–224, 1985. 14, 25

ECHER, E. Magnetosferas planetárias. **Revista Brasileira de Ensino de Física**, v. 32, n. 2, p. 1–7, 2010. 1

ECHER, E.; ZARKA, P.; GONZALEZ, W. D.; MORIOKA, A.; DENIS, L. Solar wind effects on Jupiter non-Io DAM emissions during Ulysses distant encounter (2003–2004). **Astronomy & Astrophysics**, v. 519, p. A84, 2010. 7, 29

ERGUN, R. E.; SU, Y.-J.; ANDERSSON, L.; BAGENAL, F.; DELEMERE, P. A.; LYSAK, R. L.; STRANGEWAY, R. J. S bursts and the Jupiter ionospheric Alfvén resonator. **Journal of Geophysical Research: Space Physics**, v. 111, n. A6, 2006. 14

GALOPEAU, P. H. M.; BOUDJADA, M. Y.; RUCKER, H. O. Evidence of jovian active longitude: 1. efficiency of cyclotron maser instability. **Journal of Geophysical Research: Space Physics**, v. 109, n. A12, 2004. 25, 28

GOERTZ, C. K. Io's interaction with the plasma torus. **Journal of Geophysical Research: Space Physics**, v. 85, n. A6, p. 2949–2956, 1980. 1, 2, 11, 13

GOLDREICH, P.; LYNDEN-BELL, D. Io, a jovian unipolar inductor. **The Astrophysical Journal**, v. 156, p. 59–78, 1969. 1, 2, 10, 13

GRASSET, O.; DOUGHERTY, M. K.; COUSTENIS, A.; BUNCE, E. J.; ERD, C.; TITOV, D.; BLANC, M.; COATES, A.; DROSSART, P.; FLETCHER, L. N.; HUSSMANN, H.; JAUMANN, R.; KRUPP, N.; LEBRETON, J.-P.; PRIETO-BALLESTEROS, O.; TORTORA, P.; TOSI, F.; VAN HOOLST, T. Jupiter icy moons explorer (JUICE): an ESA mission to orbit Ganymede and to characterise the Jupiter system. **Planetary and Space Science**, v. 78, p. 1–21, 2013. 18, 62

GREELEY, R.; CHYBA, C. F.; HEAD, J. W.; MCCORD, T.; MCKINNON, W. B.; PAPPALARDO, R. T.; FIGUEREDO, P. H. Geology of Europa. In: MCKINNON, W. B.; DOWLING, T. E.; BAGENAL, F. (Ed.). **Jupiter: the planet, satellites and magnetosphere**. New York: Cambridge University Press, 2004. v. 1, p. 329–362. 17, 18

GURNETT, D. A.; GOERTZ, C. K. Multiple Alfvén wave reflections excited by Io: origin of the jovian decametric arcs. **Journal of Geophysical Research: Space Physics**, v. 86, n. A2, p. 717–722, 1981. 13

HESS, S.; CECCONI, B.; ZARKA, P. Modeling of Io-Jupiter decameter arcs, emission beaming and energy source. **Geophysical Research Letters**, v. 35, n. 13, 2008. 25, 28, 29, 31, 34

HESS, S. L. G.; BONFOND, B.; ZARKA, P.; GRODENT, D. Model of the jovian magnetic field topology constrained by the Io auroral emissions. **Journal of Geophysical Research: Space Physics**, v. 116, n. A5, 2011. 41

HESS, S. L. G.; ECHER, E.; ZARKA, P. Solar wind pressure effects on Jupiter decametric radio emissions independent of Io. **Planetary and Space Science**, v. 70, n. 1, p. 114–125, 2012. 7, 31, 32

HIGGINS, C. A. Satellite control of jovian 2–6 MHz radio emission using Voyager data. **Journal of Geophysical Research: Space Physics**, v. 112, n. A5, 2007. 2, 21

HIGGINS, C. A.; CARR, T. D.; REYES, F.; GREENMAN, W. B.; LEBO, G. R. A redefinition of Jupiter's rotation period. **Journal of Geophysical Research: Space Physics**, v. 102, n. A10, p. 22033–22041, 1997. 33

HIGGINS, C. A.; MENIETTI, J. D.; CHRISTOPHER, I. W. Europa control of jovian radio emission: a Galileo study. **Geophysical Research Letters**, v. 33, n. 14, 2006. 2, 21, 22

KHURANA, K. K.; KIVELSON, M. G.; HAND, K. P.; RUSSEL, C. T. Electromagnetic induction from Europa's ocean and the deep interior. In: PAPPALARDO, R. T.; MCKINNON, W. B.; KHURANA, K. (Ed.). **Europa**. Tucson: University of Arizona Press, 2009. p. 572–586. 18, 19

KHURANA, K. K.; KIVELSON, M. G.; STEVENSON, D. J.; SCHUBERT, G.; RUSSELL, C. T.; WALKER, R. J.; POLANSKEY, C. Induced magnetic fields as evidence for subsurface oceans in Europa and Callisto. **Nature**, v. 395, n. 6704, p. 777–780, 1998. 18

KHURANA, K. K.; KIVELSON, M. G.; VASYLIUNAS, V. M.; KRUPP, N.; WOCH, J.; LAGG, A.; MAUK, B. H.; KURTH, W. S. The configuration of Jupiter's magnetosphere. In: MCKINNON, W. B.; DOWLING, T. E.; BAGENAL,

F. (Ed.). **Jupiter: the planet, satellites and magnetosphere**. New York: Cambridge University Press, 2004. v. 1, p. 593–616. 1, 2, 6

KIVELSON, M. G.; BAGENAL, F.; KURTH, W. S.; NEUBAUER, F. M.; PARANICAS, C.; SAUR, J. Magnetospheric interactions with satellites. In: MCKINNON, W. B.; DOWLING, T. E.; BAGENAL, F. (Ed.). **Jupiter: the planet, satellites and magnetosphere**. New York: Cambridge University Press, 2004. v. 1, p. 513–536. 11, 19, 20, 62

KIVELSON, M. G.; KHURANA, K. K.; VOLWERK, M. Europa's interaction with the jovian magnetosphere. In: PAPPALARDO, R. T.; MCKINNON, W. B.; KHURANA, K. (Ed.). **Europa**. Tucson: University of Arizona Press, 2009. p. 545–570. 11, 19

KRUPP, N.; KHURANA, K. K.; IESS, L.; LAINEY, V.; CASSIDY, T. A.; BURGER, M.; SOTIN, C.; NEUBAUER, F. Environments in the outer solar system. **Space Science Reviews**, v. 153, n. 1-4, p. 11–59, 2010. 2, 17

LAMY, L.; ZARKA, P.; CECCONI, B.; KLEIN, L.; MASSON, S.; DENIS, L.; COFFRE, A.; VIOU, C. 1977-2017: 40 years of decametric observations of Jupiter and the Sun with the Nançay decameter array. **arXiv preprint arXiv:1709.03821**, 2017. 35, 36, 37

LEBLANC, Y.; GERBAULT, A.; DENIS, L.; LECACHEUX, A. A catalogue of jovian decametric radio observations from January 1988 to December 1990. **Astronomy and Astrophysics Supplement Series**, v. 98, p. 529–546, 1993. 48

LECACHEUX, A. The Nançay decameter array: a useful step towards giant, new generation radio telescopes for long wavelength radio astronomy. **Radio Astronomy at Long Wavelengths**, v. 119, p. 321–328, 2000. 36

LISSAUER, J. J.; PATER, I. D. **Fundamental planetary science: physics, chemistry and habitability**. [S.l.]: Cambridge University Press, 2013. 17

LOUARN, P.; ALLEGRINI, F.; MCCOMAS, D. J.; VALEK, P. W.; KURTH, W. S.; ANDRÉ, N.; BAGENAL, F.; BOLTON, S.; CONNERNEY, J.; EBERT, R. W.; IMAI, M.; LEVIN, S.; SZALAY, J. R.; WEIDNER, S.; WILSON, R. J.; ZINK, J. L. Generation of the jovian hectometric radiation: first lessons from Juno. **Geophysical Research Letters**, v. 44, n. 10, p. 4439–4446, 2017. 29

LOUIS, C. K.; LAMY, L.; ZARKA, P.; CECCONI, B.; HESS, S. L. G. Detection of Jupiter decametric emissions controlled by Europa and Ganymede with

Voyager/PRA and Cassini/RPWS. **Journal of Geophysical Research: Space Physics**, v. 122, n. 9, p. 9228–9247, 2017. 2, 9, 21, 23, 35, 44, 47, 58, 59, 64

MARQUES, M. S. **Study of jovian high latitude radio emissions variability using 26 years of Nançay decametric array database**. 123 p. (INPE-10394-TDI/920). Thesis (PhD in Space Geophysics) — Instituto Nacional de Pesquisas Espaciais (INPE), São José dos Campos, 2017. Available from: <http://mtc-m21b.sid.inpe.br/col/sid.inpe.br/mtc-m21b/2016/10.27.08.14/doc/publicacao.pdf>. Access in: 2020. 25, 34

MARQUES, M. S.; ZARKA, P.; ECHER, E.; RYABOV, V. B.; ALVES, M. V.; DENIS, L.; COFFRE, A. Statistical analysis of 26 yr of observations of decametric radio emissions from Jupiter. **Astronomy & Astrophysics**, v. 604, p. A17, 2017. 2, 9, 22, 23, 25, 31, 32, 33, 34, 35, 36, 38, 39, 41, 44, 47, 48, 52, 60

MEILLER, V. L. F. **Ephemeris of the system III (1965) longitude of the central meridian of Jupiter**. [S.l.]: US Naval Observatory, 1980. 33

MENIETTI, J. D.; GURNETT, D. A.; KURTH, W. S.; GROENE, J. B. Control of jovian radio emission by Ganymede. **Geophysical Research Letters**, v. 25, n. 23, p. 4281–4284, 1998. 9

NEUBAUER, F. M. Nonlinear standing Alfvén wave current system at Io: theory. **Journal of Geophysical Research: Space Physics**, v. 85, n. A3, p. 1171–1178, 1980. 1, 2, 11, 12, 13

_____. Alfvén wings and electromagnetic induction in the interiors: Europa and Callisto. **Journal of Geophysical Research: Space Physics**, v. 104, n. A12, p. 28671–28684, 1999. 19

PAPPALARDO, R. T. et al. Does Europa have a subsurface ocean? Evaluation of the geological evidence. **Journal of Geophysical Research: Planets**, v. 104, n. E10, p. 24015–24055, 1999. 17, 18

PARKS, G. K. **Physics of space plasmas: an introduction**. Boulder, Colorado, USA: Westview Press, 2004. 25

PIDDINGTON, J. H.; DRAKE, J. F. Electrodynamic effects of Jupiter's satellite Io. **Nature**, v. 217, n. 5132, p. 935–937, 1968. 1, 2, 10

PRANGÉ, R.; REGO, D.; SOUTHWOOD, D.; ZARKA, P.; MILLER, S.; IP, W. Rapid energy dissipation and variability of the Io–Jupiter electrodynamic circuit. **Nature**, v. 379, n. 6563, p. 323–325, 1996. 8

QUEINNEC, J.; ZARKA, P. Io-controlled decameter arcs and Io-Jupiter interaction. **Journal of Geophysical Research: Space Physics**, v. 103, n. A11, p. 26649–26666, 1998. 31

ROTH, L.; SAUR, J.; RETHERFORD, K. D.; STROBEL, D. F.; FELDMAN, P. D.; MCGRATH, M. A.; NIMMO, F. Transient water vapor at Europa's south pole. **Science**, v. 343, n. 6167, p. 171–174, 2014. 19

SAUR, J.; NEUBAUER, F. M.; CONNERNEY, J. E. P.; ZARKA, P.; KIVELSON, M. G. Plasma interaction of Io with its plasma torus. In: MCKINNON, W. B.; DOWLING, T. E.; BAGENAL, F. (Ed.). **Jupiter: the planet, satellites and magnetosphere**. New York: Cambridge University Press, 2004. v. 1, p. 537–560. 14, 15

SHOWMAN, A. P.; MALHOTRA, R. The Galilean satellites. **Science**, v. 286, n. 5437, p. 77–84, 1999. 17

SU, Y.-J.; ERGUN, R. E.; BAGENAL, F.; DELAMERE, P. A. Io-related jovian auroral arcs: modeling parallel electric fields. **Journal of Geophysical Research: Space Physics**, v. 108, n. A2, 2003. 15

WU, C. S. Kinetic cyclotron and synchrotron maser instabilities: radio emission processes by direct amplification of radiation. **Space Science Reviews**, v. 41, n. 3-4, p. 215–298, 1985. 25

WU, C. S.; LEE, L. C. A theory of the terrestrial kilometric radiation. **The Astrophysical Journal**, v. 230, p. 621–626, 1979. 25, 28, 29

WU, C. S.; SMITH, R. A.; ZMUIDZINAS, J. S. Theory of decametric radio emissions from Jupiter. **Icarus**, v. 18, n. 2, p. 192–205, 1973. 25

ZARKA, P. Auroral radio emissions at the outer planets: observations and theories. **Journal of Geophysical Research: Planets**, v. 103, n. E9, p. 20159–20194, 1998. 1, 5, 25, 29

ZARKA, P.; FARGES, T.; RYABOV, B. P.; ABADA-SIMON, M.; DENIS, L. A scenario for jovian S-bursts. **Geophysical Research Letters**, v. 23, n. 2, p. 125–128, 1996. 14, 41

ZARKA, P.; MARQUES, M. S.; LOUIS, C.; RYABOV, V. B.; LAMY, L.; ECHER, E.; CECCONI, B. Radio emission from satellite-Jupiter interactions (especially Ganymede). In: FISCHER, G.; MANN, G.; PACHENKO, M.; ZARKA,

P. (Ed.). **Planetary radio emissions VIII**. Vienna: Austrian Academy of Sciences Press, 2017. p. 45–58. 2, 9, 22, 23, 24, 41, 42, 44, 60, 63

_____. Jupiter radio emission induced by Ganymede and consequences for the radio detection of exoplanets. **Astronomy & Astrophysics**, v. 618, p. A84, 2018. 9, 35, 44, 47, 48, 50, 60

ZIMMER, C.; KHURANA, K. K.; KIVELSON, M. G. Subsurface oceans on Europa and Callisto: constraints from Galileo magnetometer observations. **Icarus**, v. 147, n. 2, p. 329–347, 2000. 18